UNIVERSITY OF UTRECHT

DEBYE INSTITUTE

QUANTUM NANOPHOTONICS GROUP

Characterisation of Transport in Bose-Einstein Condensates Below and Above the Critical Velocity

Author:
Koen Sponselee

Supervisor:
Prof. dr. Peter van der Straten

August 5, 2016

Abstract

Five experiments are performed to characterise the time development of the chemical potential and temperature of a bimodal Bose-condensed gas. The five experiments are a stationary experiment, a slow motion experiment, a slow motion over a barrier experiment, a fast motion experiment and a fast motion over a barrier experiment. In the two slow motion experiments the atoms are moved with velocities below the critical velocity of superfluidity, while in the two fast motion experiments the atoms are moved with velocities above the critical velocity. We observed superfluidity in the slow slow motion experiments. Additional heating was observed in fast motion experiments, indicating that the system is not superfluid in this regime.

Furthermore we find transition temperatures for the five experiments. Below this transition temperature, heating of the system occurs and above, cooling of the system occurs. For the stationary experiment, the transition temperature is found to be approximately 719 nK.

Contents

1 Introduction

In 1924 Satyendra Bose derived the black-body spectrum found earlier by Planck by solely using statistical arguments. Having trouble getting this paper published, Bose sent his work to Einstein. Einstein understood the importance of Bose's work, translated the work to German himself and extended it to apply to massive non-interacting particles. Einstein predicted that below a finite critical temperature integer-spin particles, later called bosons, make a phase transition to a new phase. This leads to a macroscopic occupation of the single-particle ground state of the system. This new state of matter became known as a Bose-Einstein condensate (BEC) [1–3].

It took just over 70 years to achieve Bose-Einstein condensation of atoms experimentally. In 1995, it was first observed in rubidium atoms in the NIST-JILA lab by Cornell and Wieman [1]. Later that year, it was achieved in sodium atoms at MIT by Ketterle's group [2]. It has been the subject of much research around the world ever since and nowadays Bose-Einstein condensation has been observed in among others different alkali atoms, hydrogen, molecules and photons [3, 4].

Bose-Einstein condensates form an interesting research field especially because it can be controlled very precisely in the lab. It allows one to study macroscopic quantum mechanical behaviour of a system accurately, which is often difficult in large systems at higher temperatures. Furthermore, theoretical predictions can be calculated accurately and therefore theory and experiment can be compared accurately. It thus forms a model system for various exotic phenomena in other systems.

The research presented in this work is aimed at characterising transport properties of the BEC. To describe the properties of the condensate, we will study the chemical potential and temperature of the system. These are our quantities of interest. The two quantities will be able to describe the system using simple assumptions. The time development of the chemical potential and temperature of atomic clouds below the critical temperature will be studied. This will be done for different transport experiments. A core concept in quantum transport, or hydrodynamics, is superfluidity, which is flow with zero viscosity. Below a critical velocity, the BEC behaves like a superfluid and we therefore expect the system will not behave differently from stationary experiments. Above this critical velocities, excitations can be made, increasing the energy of the system. Therefore, we expect that in these experiments we will observe an increase in energy. Our goal is to characterise the temporal behaviour of our quantities of interest for different transport experiments, and to compare this for different transport experiments below and above the critical velocity.

This thesis is structured in the following way: in Sec. 2 the essential theory will be explained, in Sec. 3 the experimental methods will be described and justified, in Sec. 4 the results will be presented and in Sec. 5 the results will be discussed.

2 Theory

The theory of Bose-Einstein condensation is explained in detail in textbooks [3,5] and is discussed briefly in Sec. 2.1. A short explanation is given in Sec. 2.2 and Sec. 2.3, mostly focussing on relating the column densities and total number of particles to the chemical potential and temperature. The atomic cloud between absolute zero and the critical temperature is discussed in Sec. 2.4 and a brief overview for the criteria for superfluid properties are given in Sec. 2.5. Furthermore, a theoretical description of the imaging technique is given in Sec. 2.6.

2.1 The Ideal Bose Gas

The field of Bose-Einstein condensation is focussed on systems of many particles. To obtain thermodynamic properties of a system of those particles, the grand partition function must be found. Assuming a system of non-interacting massive bosons, the grand partition function $\mathcal{Z}$ is given by

$$\mathcal{Z} = \Pi_{\vec{k}}\, \mathcal{Z}_{\vec{k}}, \tag{2.1}$$

where $\vec{k}$ is the wavevector of a particle, and where the single particle partition function $\mathcal{Z}_{\vec{k}}$ is given by

$$\mathcal{Z}_{\vec{k}} = \frac{1}{1 - \mathrm{e}^{-\beta(E_{\vec{k}} - \mu)}}, \tag{2.2}$$

where $\beta = 1/k_{\mathrm{B}}T$ with k_{B} the Boltzmann constant and T the temperature, $E_{\vec{k}}$ is the energy of a particle with wave vector $\vec{k}$ and μ is the chemical potential of the system [6].

Using the grand partition function, the number of particles N can be obtained by [6]

$$N = k_{\mathrm{B}}T \frac{\partial}{\partial \mu} \ln \mathcal{Z}. \tag{2.3}$$

Using Eq. 2.1 and Eq. 2.2, this can be rewritten as [6]

$$N = k_\mathrm{B} T \sum_{\vec{k}} \frac{\partial}{\partial \mu} \ln(\mathscr{Z}_{\vec{k}}),$$

$$= -k_\mathrm{B} T \sum_{\vec{k}} \frac{\partial}{\partial \mu} \ln\left(1 - \mathrm{e}^{-\beta(E_{\vec{k}} - \mu)}\right), \tag{2.4}$$

$$= \sum_{\vec{k}} \frac{1}{\mathrm{e}^{\beta(E_{\vec{k}} - \mu)} - 1}.$$

Note that here the chemical potential must be negative, such that the particle number does not diverge. In the thermodynamic limit, this summation can be rewritten as

$$N = \int_0^\infty \mathrm{d}E \, \mathcal{D}(E) \, \frac{1}{\mathrm{e}^{\beta(E - \mu)} - 1}, \tag{2.5}$$

where $\mathcal{D}(E)$ is the density of states [6]. For many systems, such as a uniform or a harmonic oscillator potential, the density of states is of the form

$$\mathcal{D}_\alpha(E) = C_\alpha E^{\alpha - 1}, \tag{2.6}$$

where α and C_α are constants depending on the system [3]. Introducing the *fugacity* $z = \mathrm{e}^{\beta \mu}$, Eq. 2.5 can be rewritten as

$$N = C_\alpha \int_0^\infty \mathrm{d}E \, \frac{E^{\alpha - 1}}{z^{-1} \mathrm{e}^{\beta E} - 1}. \tag{2.7}$$

This integral can be rewritten in terms of the dimensionless parameter $x = \beta E$ such that

$$N = C_\alpha (k_\mathrm{B} T)^\alpha \int_0^\infty \mathrm{d}x \, \frac{x^{\alpha - 1}}{z^{-1} \mathrm{e}^x - 1},$$
$$= C_\alpha (k_\mathrm{B} T)^\alpha \, \Gamma(\alpha) \, g_\alpha(z), \tag{2.8}$$

where the gamma function is $\Gamma(\alpha) = \int_0^\infty \mathrm{d}x x^{\alpha - 1} \mathrm{e}^{-x}$ and the Bose function is $g_\alpha(z) = \sum_{n=1}^\infty z^n / n^\alpha$ [6]. For a three-dimensional uniform system, $\alpha = 3/2$ and $C_\alpha = V m^{3/2} / \sqrt{2} \pi^2 \hbar^3$ [3]. The particle density $n = N/V$ of a three-dimensional uniform system is given by

$$n = \frac{(m k_\mathrm{B} T)^{3/2}}{\sqrt{2} \pi^2 \hbar^3} \, \Gamma(3/2) \, g_{3/2}(z). \tag{2.9}$$

Using that $\Gamma(3/2) = \sqrt{\pi}/2$ and introducing the thermal de Broglie wavelength $\lambda_{\text{th}} = \sqrt{2\pi\hbar^2/mk_{\text{B}}T}$, Eq. 2.9 can be rewritten as

$$n\lambda_{\text{th}}^3 = g_{3/2}(z). \tag{2.10}$$

As discussed before, the chemical potential must be negative. Under this constraint, the Bose function has a maximum as $\mu \to 0$. In that case, the Bose function reduces to the Riemann zeta function $\zeta(\alpha) = \sum_{n=1}^{\infty} n^{-\alpha}$ such that $g_{3/2}(1) = \zeta(3/2) \approx 2.612$ [6,7]. The right-hand side of Eq. 2.10 thus has a finite maximum. However, the left-hand side can be increased further, by either increasing the density or decreasing the temperature. At the critical temperature T_{c}

$$n \left(\frac{2\pi\hbar^2}{mk_{\text{B}}T_{\text{c}}} \right)^{3/2} = \zeta(3/2) \approx 2.612. \tag{2.11}$$

As the temperature is decreased below T_{c} or as the density is increased, the derivation thus fails. This is when Bose-Einstein condensation occurs. The ground state of the system is not properly accounted for in going from the summation to the integral in Eq. 2.5.

Below T_{c} the ground state becomes macroscopically occupied and the atoms in the ground state are said to be in the condensate. The atoms in excited states are said to be in the thermal cloud. To describe this, the total number of particles N_{tot} is given by $N_{\text{tot}} = N_{\text{th}} + N_{\text{c}}$, where N_{th} is the number of particles in the thermal cloud and N_{c} is the number of particles in the condensate [3,5,6].

2.2   The Thermal Cloud

To obtain the particle density of the thermal cloud in an external potential, the chemical potential must be be replaced by $\mu - V_{\text{ext}}(\vec{r})$, where $V_{\text{ext}}(\vec{r})$ is the potential energy function at position $\vec{r}$. Using Eq. 2.10 the particle density of the thermal cloud is given by

$$n_{\text{th}}(\vec{r}) = \frac{1}{\lambda_{\text{th}}^3} g_{3/2} \left(e^{(\mu - V_{\text{ext}}(\vec{r}))/k_B T} \right). \tag{2.12}$$

Below the critical temperature T_c at which Bose-Einstein condensation occurs, the chemical potential of the thermal cloud is zero, as seen in Sec. 2.1. In our experimental setup, atoms are trapped in an external potential that is to good approximation harmonic in the centre of the trap. This harmonic potential is described by

$$V_{\text{ext}}(\vec{r}) = \frac{1}{2}m\left(\omega_x^2 x^2 + \omega_y^2 y^2 + \omega_z^2 z^2\right), \tag{2.13}$$

where ω_i are the trap frequencies in the $i \subset \{x, y, z\}$ directions.

In the experiment, the column densities of the atoms is measured. To extract the column density from the density distribution n_{th}, the imaged direction must be integrated out. In our setup, this is the y-direction. The column density $\rho_{\text{th}}(x, z)$ can be written as

$$\begin{aligned}
\rho_{\text{th}}(x, z) &= \int_{-\infty}^{\infty} n_{\text{th}}(x, y, z)\, \mathrm{d}y \\
&= \frac{1}{\lambda_{\text{th}}^3} \int_{-\infty}^{\infty} g_{3/2}\left(e^{\left(-m(\omega_x^2 x^2 + \omega_y^2 y^2 + \omega_z^2 z^2)/2\right)/k_B T}\right)\, \mathrm{d}y \\
&= \frac{1}{\lambda_{\text{th}}^3} \int_{-\infty}^{\infty} \sum_{n=1}^{\infty} \frac{1}{n^{3/2}} e^{n\left(-m(\omega_x^2 x^2 + \omega_y^2 y^2 + \omega_z^2 z^2)/2\right)/k_B T}\, \mathrm{d}y \\
&= \frac{1}{\lambda_{\text{th}}^3} \sqrt{\frac{2k_B T}{m\omega_y^2}} \sqrt{\pi}\, g_2\left(e^{\left(-m(\omega_x^2 x^2 + \omega_z^2 z^2)/2\right)/k_B T}\right).
\end{aligned} \tag{2.14}$$

In our experiment, the trap is cylindrically symmetric, and therefore $\omega_x = \omega_y$ [8]. Using that $\lambda_{\text{th}} = \sqrt{2\pi\hbar^2/mk_B T}$, the column density as a function of position and temperature is given by

$$\rho_{\text{th}}(x, z, T) = \frac{mk_B^2}{2\pi\hbar^3\omega_x} T^2\, g_2\left(e^{-m\left(\omega_x^2 x^2 + \omega_z^2 z^2\right)/2k_B T}\right). \tag{2.15}$$

For given ω_i, the number of particles in the thermal cloud is only a function of temperature. The number of particles in the thermal cloud N_{th} is determined by integrating the column density over the x- and z-directions as [5, 7]

$$N_{\text{th}}(T) = \int_{-\infty}^{\infty} \int_{-\infty}^{\infty} \rho_{\text{th}}(x, z)\, \mathrm{d}x\, \mathrm{d}z = \frac{k_B^3 \zeta(3)}{\hbar^3 \omega_x^2 \omega_z} T^3. \tag{2.16}$$

2.3 The Bose-Einstein Condensate

A pure BEC at zero temperature can be described by the order parameter ψ that satisfies the time-independent Gross-Pitaevskii equation (GPE)

$$\left(-\frac{\hbar^2}{2m}\vec{\nabla}^2 + V_{\text{ext}}(\vec{r}) + V_{\text{self}}\left|\psi(\vec{r})\right|^2\right)\psi(\vec{r}) = \mu\psi(\vec{r}), \tag{2.17}$$

where V_{ext} is the external potential, $V_{\text{self}} = 4\pi\hbar^2 a/m$ is a coupling constant with a the scattering length, and $\left|\psi(\vec{r})\right|^2$ is the atom density. The first term is the kinetic energy term and the second term is the potential energy term. The third term of the GPE takes into account the mean field potential caused by the atoms. This is a mean field description and it therefore works well if the system has many particles. In the experiment described in this thesis, the number of particles in the condensed state is typically 15 million, for which this description can be applied accurately [3, 7].

Under the Thomas-Fermi approximation, the kinetic term of the GPE is neglected. This is a good approximation in the limit of strong interactions or small momenta. The condensate number density $n_c(\vec{r})$ as function of the position $\vec{r}$ is given by [7]

$$n_c(\vec{r}) = \left|\psi(\vec{r})\right|^2 = \max\left(\frac{\mu - V_{\text{ext}}(\vec{r})}{V_{\text{self}}}, 0\right). \tag{2.18}$$

Using Eq. 2.13 this can be rewritten as

$$n_c(\vec{r}) = \frac{\mu}{V_{\text{self}}} \max\left(1 - \frac{m\left(\omega_x^2 x^2 + \omega_y^2 y^2 + \omega_z^2 z^2\right)}{2\mu}, 0\right). \tag{2.19}$$

As for the thermal cloud, the column densities of the atoms are measured in the experiment. To extract the column densities from the density distribution n_c, the y-direction is integrated out. The column density of the condensate $\rho_c(x, z)$ can be written as

$$\begin{aligned}
\rho_c(x, z) &= \int_{-\infty}^{\infty} n_c(x, y, z)\, dy \\
&= \frac{\mu}{V_{\text{self}}} \int_{-\infty}^{\infty} \max\left(1 - \frac{m\left(\omega_x^2 x^2 + \omega_y^2 y^2 + \omega_z^2 z^2\right)}{2\mu}, 0\right) dy \\
&= \frac{\mu}{V_{\text{self}}} \frac{4}{3} \sqrt{\frac{2\mu}{m\omega_y^2}} \max\left(1 - \frac{m\left(\omega_x^2 x^2 + \omega_z^2 z^2\right)}{2\mu}, 0\right)^{3/2}.
\end{aligned} \tag{2.20}$$

Using that our trap is cylindrically symmetric, and using that $V_{\text{self}} = 4\pi\hbar^2 a/m$ [7] this can be rewritten as a function of position and the chemical potential as

$$\rho_c(x, z, \mu) = \frac{\sqrt{2m}}{3\pi\hbar^2 a\omega_x} \mu^{3/2} \max\left(1 - \frac{m\left(\omega_x^2 x^2 + \omega_z^2 z^2\right)}{2\mu}, 0\right)^{3/2}. \tag{2.21}$$

For given ω_i and a, the number of particles in the condensate is only a function of

the chemical potential. The number of particles in the condensate N_c is obtained by integrating the column density over the x- and z-directions as

$$N_c(\mu) = \int_{-\infty}^{\infty} \int_{-\infty}^{\infty} \rho_c(x,z) \, \mathrm{d}x \, \mathrm{d}z = \frac{4\sqrt{2}}{15} \frac{1}{a\sqrt{m}\hbar^2 \omega_x^2 \omega_z} \mu^{5/2}. \tag{2.22}$$

2.4 Bimodal Density Distributions

Below T_c, but above absolute zero, the atomic cloud consists of a condensate and a thermal part. Such a system is referred to as a bimodal cloud. The condensate fraction N_c depends on the temperature as [3,5]

$$\frac{N_c(T)}{N_{tot}} = 1 - \left(\frac{T}{T_c}\right)^{\alpha} \tag{2.23}$$

Section 2.2 describes the limit where $T \to T_c$, while Sec. 2.3 describes the limit where $T \to 0$. Therefore, between absolute zero and T_c a different approach is needed.

To properly take into account the effect of finite temperature, one needs to take into account the effect of interactions between the condensate atoms and the thermal atoms. This can be done in several ways, three of which are demonstrated in Ref. [9]. A first approximation is to neglect all interactions. In this work, this non-interacting model is assumed, such that $\rho = \rho_c + \rho_{th}$. This has the advantage that the column density can be obtained analytically, which cannot be done when including interactions. Even though interactions must be present to achieve Bose-Einstein condensation, these results will be a good first approximation for large weakly-interacting systems.

Figure 2.1 shows the total column density for our experimental trap frequencies and for typical temperature and chemical potential. The thermal cloud is the broad and low distribution and the BEC is the narrower and higher paraboloid-like distribution on top. The total column density is continuous, but the position derivative has a discontinuity at the edge of the condensate, as can be seen by examining Eq. 2.21. This feature can be used to visually identify if a condensate is present.

2.5 Superfluidity & Critical Velocity

A superfluid is a fluid that flows with zero viscosity. It experiences no friction and is rotationless. A Bose-Einstein condensate behaves like a superfluid if its velocity is smaller than a critical velocity. Above this critical velocity, excitations can be created. These excitations can among others be solitons, sound waves or vortices. Vortices
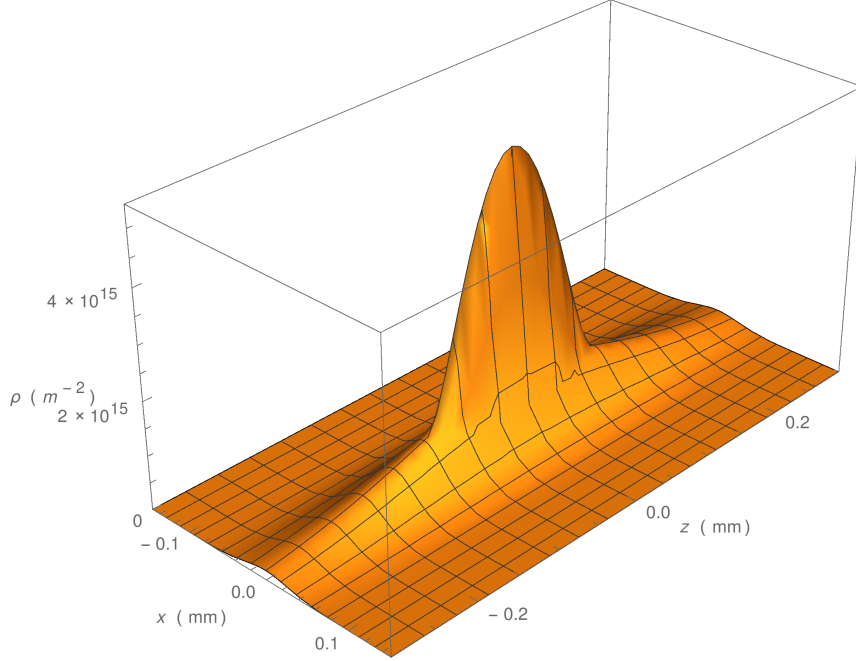
Figure 2.1: Total column density as a function of position assuming a non-interacting model, for a bimodal cloud of sodium atoms with temperature 700 nK and chemical potential 3.0 kHz, and using the trap frequencies $\omega_x = 2\pi \cdot 92.5$ Hz and $\omega_z = 2\pi \cdot 15.3$ Hz as in our experiment.

are phase singularities. The condensate phase increases with 2π when going through a loop around a vortex, while the density is zero in the centre of the vortex [3, 10].

The critical velocity is to good approximation equal to the velocity of sound for ultra-cold atomic systems with weak interactions. The speed of sound v_s is defined by

$$mv_s^2(\vec{r}) = \mu - V_{\text{ext}}(\vec{r}). \tag{2.24}$$

This reduces to $v_s(\vec{r}) = v_s = \sqrt{\mu/m} = \sqrt{V_{\text{self}} n_c/m}$ for a uniform system [11]. Since the experiments are done in a harmonic trap, this needs to be modified. For a cylindrically symmetric trap with $\omega_{x,y} \gg \omega_z$, the condensate density needs to be replaced by $n_c(0, 0, z)/2$. Therefore, the speed of sound in the elongated trap is given by [11]

$$v_{\mathrm{s}}(z) = \sqrt{\frac{V_{\mathrm{self}}\, n_{\mathrm{c}}(0,0,z)}{2m}}. \tag{2.25}$$

In the experiment, the initial chemical potential of the cloud is typically between $3\,\mathrm{kHz}$ and $4\,\mathrm{kHz}$ in units of h. This yields a speed of sound in the centre of the cloud between approximately 5.1 mm/s and 5.9 mm/s, respectively.

2.6   Phase-Contrast Imaging

Studying the density distribution of an ultra-cold atomic cloud is done by measuring its column density with a probe beam. The absorption imaging technique uses resonant light. The light shines on the atomic cloud and casts a shadow on the camera behind the atomic cloud. Shining resonant light on the ultra-cold cloud causes it to heat up and destroys the sample. Therefore a new cloud has to be prepared for each measurement. Large shot-to-shot variations in, for example, the number of trapped particles make this measuring method disadvantageous compared to other techniques when studying time-dependent behaviour of a condensate.

The measuring method used in this experiment is called *Phase-Contrast Imaging* (PCI) and it is non-destructive because it uses off-resonant light. The basic idea behind PCI is to shine a part of the off-resonant light on the atomic cloud, accumulating an additional phase through the light-atom interaction. The more atoms the light interacts with, the larger the accumulated phase is. This part of the light is interfered with another part of the light that is focussed on a phase spot behind the atoms where it accumulates a constant phase shift. This way, the interference pattern will contain the information about the column density [8,12].

The PCI technique is strictly speaking not *non*-destructive as a small part of the atoms is still lost. Rather, few atoms are lost compared to absorption imaging and generally dozens of images can be taken from the same condensate. For large detuning of the light with respect to the ground to excited state transition, and for negligible saturation, the scattering rate R_{sc} is given by

$$R_{\mathrm{sc}}(\vec{r}) = \frac{3\pi c^2}{2\hbar\omega_0^3} \left(\frac{\omega}{\omega_0}\right)^3 \left(\frac{\Gamma}{\omega_0 - \omega} + \frac{\Gamma}{\omega_0 + \omega}\right)^2 I(\vec{r}), \tag{2.26}$$

where c is the speed of light in vacuum, ω_0 is the frequency of the atom ground to excited state transition, ω is the frequency of the laser, Γ is the natural linewidth of atomic transition and I is the light intensity [13].

The detuning is defined as $\delta = \omega - \omega_0$. Assuming that the detuning is much smaller than the ground to excited state frequency, the rotating wave approximation can be used to rewrite Eq. 2.26 as [13]

$$R_{\text{sc}}(\vec{r}) = \frac{3\pi c^2}{2\hbar\omega_0^3}\left(\frac{\Gamma}{\delta}\right)^2 I(\vec{r}). \tag{2.27}$$

Notice that the scattering rate is proportional to $I\delta^{-2}$. Increasing the detuning thus reduces the scattering. However, the phase shift is related to the dispersion, which is proportional to $I\delta^{-1}$. In our experiment, the intensity and detuning are chosen such that the scattering rate is small and dozens of images can be taken, while the phase shift is still measurable [8, 12].

The electric field of the probe beam accumulates an extra phase when passing through the atoms; another part of the light accumulates an extra phase when passing the phase spot. After the phase spot, the electric field E is given by

$$E(x, z) = E_0 e^{i\theta} + E_0\left(e^{i\phi(x,z)} - 1\right), \tag{2.28}$$

where E_0 is the absolute value of the electric field before passing through the atoms and phase spot, θ is the phase that the light accumulates when passing through the phase spot and ϕ is the phase that the light accumulates when passing through the atoms [12]. If the light passes no atoms on a position (x, z), $\phi = 0$ and the second term becomes 0. In that case, the electric field only accumulates a phase θ due to the phase spot and the measured intensity is the same as the probe beam intensity. The intensity I is proportional to the absolute value squared of the electric field, such that the intensity is related to ϕ as

$$I = I_0\left[3 - 2\cos\left(\theta\right) + 2\cos\left(\theta - \phi\right) - 2\cos\left(\phi\right)\right], \tag{2.29}$$

where I_0 is the probe beam intensity profile [12].

The signal S that is measured in the experiments is given by

$$S(x, z) = \frac{I(x, z)}{I_0(x, z)}. \tag{2.30}$$

When measuring the intensities, any ambient background light will also contribute to the signal. Therefore, the intensity of the background light must be substracted from both of the intensities. The signal in measured quantities is given by

$$S(x, z) = \frac{I(x, z) - I_{\text{bg}}(x, z)}{I_0(x, z) - I_{\text{bg}}(x, z)}, \tag{2.31}$$

where I_{bg} is the intensity as measured without the atoms and without the probe light on. All the intensities are functions of the position in the x, z-plane [8, 12].

Measuring the intensities given in Eq. 2.31 yields the signal. Using Eq. 2.29 these measured quantities can be related to the phase accumulated due to the atoms

$$S\big(\phi(x,z)\big) = 3 - 2\cos(\theta) + 2\cos(\theta - \phi(x,z)) - 2\cos(\phi(x,z)).\qquad(2.32)$$

Equation 2.32 is plotted in Fig. 2.2 for three values of the phase spot θ. Note that for $\theta = \pi/3$, the signal lies between 0 and 4.
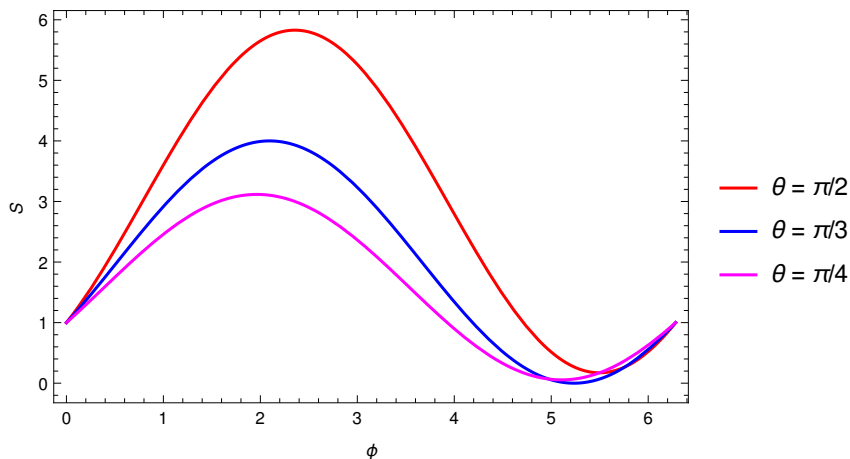

Figure 2.2: The signal S as a function of the phase ϕ (in radians) given by Eq. 2.32, plotted for three different values of phase spot θ.

The phase is related to the particle density $n(x,y,z)$ as

$$\phi(x,z) = k \int_{-\infty}^{\infty} \left(\sqrt{1 + \frac{n(x,y,z)\alpha/\epsilon_0}{1 - n(x,y,z)\alpha/3\epsilon_0}} - 1 \right) \mathrm{d}y,\qquad(2.33)$$

where $k = 2\pi/\lambda$ is the wave vector, α is the polarizability of the atoms and ϵ_0 is the permittivity of vacuum [8,9]. For $|n\alpha/\epsilon_0| \ll 1$ this can be approximated by

$$\phi(x,z) = \frac{k\alpha}{2\epsilon_0} \int_{-\infty}^{\infty} n(x,y,z)\,\mathrm{d}y = \frac{k\alpha}{2\epsilon_0}\,\rho(x,z),\qquad(2.34)$$

which relates the column density to accumulated phase [8,9].

In our experiment, the trapped sodium atoms are in the $\big|F_g, M_g\big\rangle = \big|1, -1\big\rangle$ state. If we assume the detuning δ of the probe light with respect to the $F_g \to F_e$ transition is large, and if we assume the detuning is approximately the same for the transitions to all excited states, the polarizability is given by

$$\alpha = -\frac{\epsilon_0 c \Gamma \sigma_\lambda}{3\omega\delta},$$ (2.35)

where ϵ_0 is the vacuum permittivity and σ_λ is the cross section of light absorption [9].

For our experiment, the phase and the column density are thus related as

$$\phi(x,z) = -\frac{\sigma_\lambda \Gamma}{6\delta}\,\rho(x,z).$$ (2.36)

With this relation between the phase and the column density, and using the assumption from Sec. 2.4 for the total column density and the results from Sec. 2.2 and Sec. 2.3, a relation between the measured signal and the chemical potential and temperature is found.

3 Methods

The experimental setup used for this work is explained in detail in Refs. [8, 12, 14]. In Sec. 3.1 the analysis of the experimental data is explained, in Sec. 3.2 the method used to displace the atomic cloud is explained and in Sec. 3.3 the creation of a barrier and the additions to the setup are explained. Finally, Sec. 3.4 gives an overview of the experiments that are done for this thesis.

3.1 PCI Analysis

The PCI measuring technique as explained in Sec. 2.6 is used to study the column density distribution of the BEC and thermal cloud. In our experiment, the probe light has a power of $50\,\mu W$ and an $80\,\mu s$ illumination time, and a detuning of $-350\,MHz$ with respect to the ground to excited state transition. A typical PCI image can be seen in Fig. 3.1a. The signal is close to one far off the centre. At that position, the accumulated phase is approximately zero and therefore also the atom density is approximately zero. Closer to the centre, the signal first increases slowly and then rapidly as the signal reaches its maximum. The signal drops to below one even closer to the centre and becomes close to zero. Here, the accumulated phase is largest and therefore the atom density is highest on that position. The rapid increase of accumulated phase indicates the edge of the condensate, as discussed in Sec. 2.4.

The data is acquired by measuring 3 series of images. The first series of images consists of 40 measurement of the intensity of the probe light as it passes through the cloud of trapped atoms. The second series of 40 images is taken by measuring the intensity of the probe light without the trapped atoms. The third series of 40 images is taken by measuring the intensity of the background light with the probe beam off. These three series correspond to $I(x, z)$, $I_0(x, z)$ and $I_{bg}(x, z)$ from Eq. 2.31, respectively, and are used to determine the signal.

Because the different intensities are measured at different times, fluctuations in the probe light intensity and fluctuations in the background light can cause a global error in the signal, which is different for each PCI image. It is observed in many measurements that the background signal became constant at values significantly higher than one. This implies that such a fluctuation is present. To compensate for this, the signal background is determined by averaging a 20 by 20 pixel corner of the signal without atoms. The entire image is divided by this average, such that the signal goes down to one at the edges. Furthermore, due to misalignment of the phase spot and due to statistical uncertainties in the measured intensities, the measured signal sometimes reached values larger than expected from Eq. 2.32. To compensate for this, the signal data is capped at the maximum that the signal reaches theoretically.

The analysis was done by fitting the signal as given in Eq. 2.32 for given phase spot

θ. In Sec. 2.4 interactions are neglected and we assumed the total column density is the sum of the thermal and condensate column densities. The Bose function $g_{3/2}$ was approximated in this fitting procedure by only taking into account the first two terms of the infinite sum. The other terms only give a relatively small contribution. Furthermore a coordinate transformation was done to correct for the small angle between the imaged axis and the long axis of the atomic cloud, and to take into account that the cloud is not centred around the origin. Therefore, the five independent fitting parameters are the temperature, the chemical potential, the x- and z-position of the centre and the angle between the imaged z-axis and the long axis of the atomic cloud. A Levenberg-Marquardt algorithm was used for fitting, which is an unconstrained fitting algorithm.

The phase spot used in the experiment was $\pi/3$. For this particular phase spot, the maximum signal is 4 and the minimum is 0. The signal as a function of the phase is plotted in Fig. 2.2 for different values of θ. It can be seen that the maximum signal of the data in Fig. 3.1a lies around three before the signal decreases towards zero in the centre. This behaviour is also seen in all other runs. A maximum signal of four is expected with a $\pi/3$ phase spot. Since it is unexpected that the column density has any discontinuities, we do not expect the maximum to be three while it also goes back towards zero close to the centre. Figure 3.1b shows a fit to the measurement data using $\theta = \pi/3$. In comparison, Fig. 3.1c shows a fit done assuming a $\pi/4$ phase spot, for which the maximum goes to about 3.1. The fit with $\theta = \pi/4$ describes the data significantly better than the fit with $\pi/3$. We therefore assume the phase spot is $\pi/4$ from now on.

We have observed that the alignment of the phase spot is very critical. It is possible that due to a slight misalignment our probe beam is not focussed perfectly on the centre of the phase spot and that a small fraction of the focussed light just misses the phase spot. This can explain why the phase spot effectively acts like a $\pi/4$ phase spot.

The position of the centre of the atomic cloud is generally determined with a fitting uncertainty of approximately $0.25\,\mu$m. The deviation of the position between PCI images was generally up to $2.5\,\mu$m for stationary experiments. However, towards the end of the experiment, the fits sometimes found the centre at least $20\,\mu$m away from the previous position. In these cases, the fit also found a decrease in chemical potential of 1 kHz or more, while the decrease is generally up to 0.2 kHz between PCI images. In a stationary experiment such large jumps are not expected, and it was observed that the fits did not describe the data well in these cases. Therefore, we chose to reject fits to images in stationary experiments if the centre position deviated more than $10\,\mu$m from the previous position and if the chemical potential deviated by more than 1 kHz from the previous chemical potential.

In experiments where the atomic cloud is moved, this procedure did not work, since in those experiments a displacement of the centre is expected. Instead, the found
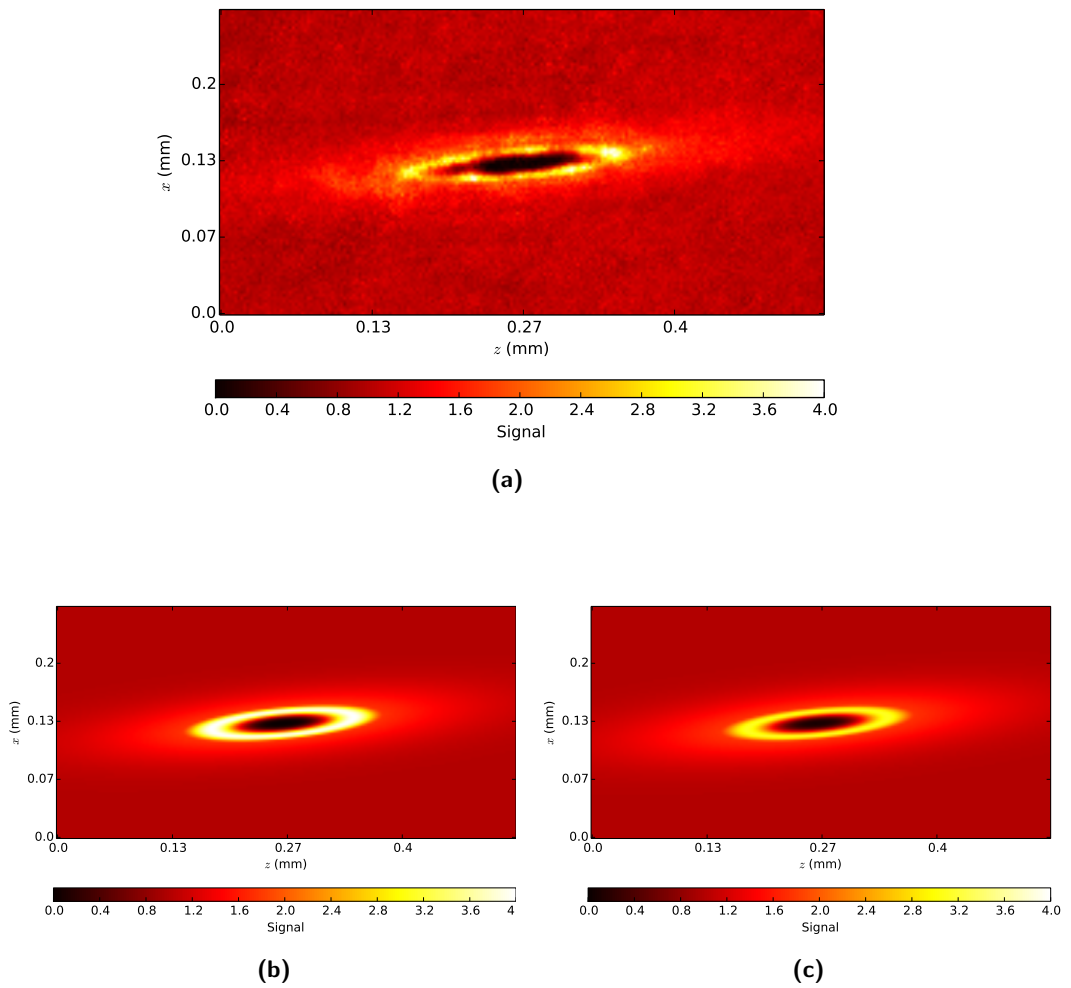
(a)

(b)

(c)

Figure 3.1: (a) shows a typical image as obtained by a PCI measurement, (b) shows the best fit assuming $\theta = \pi/3$ and (c) shows the best fit assuming $\theta = \pi/4$. On the horizontal axis, the z-position is plotted, on the short axis the x-position is plotted and the colour bar indicates the height of the measured signal. The data is significantly better described assuming a $\pi/4$ phase spot. Assuming a $\pi/4$ phase spot for this measurement, the chemical potential was found to be 3.458 ± 0.004 kHz, the temperature was found to be 637.1 ± 1.2 nK and the total number of particles for this atomic cloud was determined at $35 \cdot 10^6$.

position is compared to the guessed value of the position. For dense clouds, the signal is below 1, as seen in Fig. 3.1a. If the minimum of the signal was significantly below the background of 1, the position of the minimum is used as the initial guess for the fit. Otherwise, the position of the maximum of the signal is used as the initial guess. If the deviation of the fitted centre position from the initially guessed position is larger than 15 μm and if the deviation from the previous chemical potential is larger than 1 kHz, the fit was rejected.

Furthermore, the fit is rejected if the chemical potential becomes negative, because this experiment is aimed at studying the temporal behaviour above T_c. Using these rejection criteria worked well and ensured that only fits were accepted that described the data well. A fit to a typical bimodal cloud can be seen in Fig. 3.2.
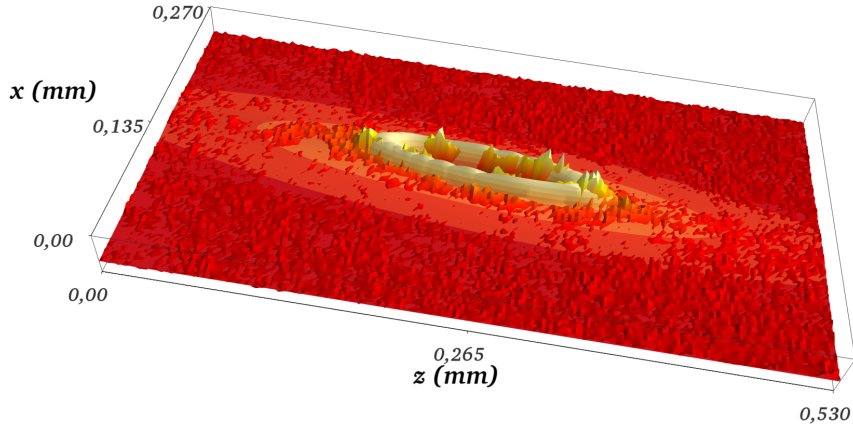

Figure 3.2: A 3D plot of the data together with the fitted surface, assuming a $\pi/4$ phase spot. The 'rough' points indicate the data, while the smooth surface with the contour lines shows the best fitted surface. On the horizontal axis, the z-position is plotted, on the short axis the x-position is plotted and the colour and height indicates the height of the measured signal. The data plotted here is the same as the data plotted in Fig. 3.1a.

3.2   BEC Displacement

The atomic cloud is trapped in a harmonic potential using magnetic fields created by electromagnetic coils. By changing the current through these coils, the minimum of the harmonic trap is moved. Changing the current thought the MOT coils results in a gradient force acting on the atomic cloud in the z'-direction. Here the z'-direction is taken to be the BEC axis, which is under an angle of approximately 5 degrees with the imaged axis. For details on the coils, see Refs. [8] and [12].

If the current is ramped very slowly, the atomic cloud will get a small displacement

16

and follow the movement of the minimum of the trap, but if the current is ramped very quickly, the atomic cloud will start to oscillate around the new centre. When moving slowly, the system will have time to adjust to the new minimum. However, when moving quickly the system will not have time to adjust to the new minimum immediately. Instead, it will undergo a rise in potential and it will start to oscillate around a minimum that is displaced with respect to the original minimum.

To achieve the slow motion, the current through the MOT coils was ramped linearly from 4.0 A to 2.1 A in 500 ms. To achieve the fast motion, the current through the MOT coils was ramped linearly from 4.0 A to 0.6 A in 25 ms. These are referred to as the slow and fast current ramps, respectively.

The effect of these two types of current ramps is shown in Fig. 3.3. In Fig. 3.3a the z'-component of the position as a function of time is shown for the slow current ramp. The position is seen to increase and it increases less quickly as it progresses. A parabola was fitted to describe the position as a function of time. The maximum velocity was estimated by determining the derivative of the position at $t = 0$ ms and was found to be $v_{\max} = 0.14 \pm 0.03$ mm/s, much smaller than the lower bound of the critical velocity of 5.1 mm/s (see Sec. 2.5). In Fig. 3.3b the z'-component of the position is shown for the fast current ramp. The position is seen to oscillate. A sine was fitted to describe the position as a function of time and this describes the data very well. Note that the first point, at $t = 0$ ms, is not described well by the sine. This is because at that time the BEC is still situated at the original potential minimum. For the fast current ramp, the maximum velocity was determined to be $v_{\max} = 9.8 \pm 0.3$ mm/s, which is larger than the upper bound on the critical velocity of 5.9 mm/s of our experiment.

In both cases the motion in the perpendicular direction was observed to be negligible and therefore the estimates of these maximum velocities gave a good estimate of the real maximum velocity.

3.3   The Light Barrier

A 532 nm green laser was used to create a repelling barrier for the BEC. The laser has a maximum laser output power of 1.5 W and is tunable in steps of 2 mW. This laser acts as an optical dipole trap and creates a potential U

$$U = \frac{3\pi c^2}{2\omega_0^3} \frac{\Gamma}{\delta} I, \tag{3.1}$$

where ω_0 is the frequency of the transition between the ground and excited state and $\delta = \omega - \omega_0$ is the detuning of the laser with frequency ω with respect to the transition frequency ω_0 [8]. For the blue-detuned laser, δ is positive and U is positive.
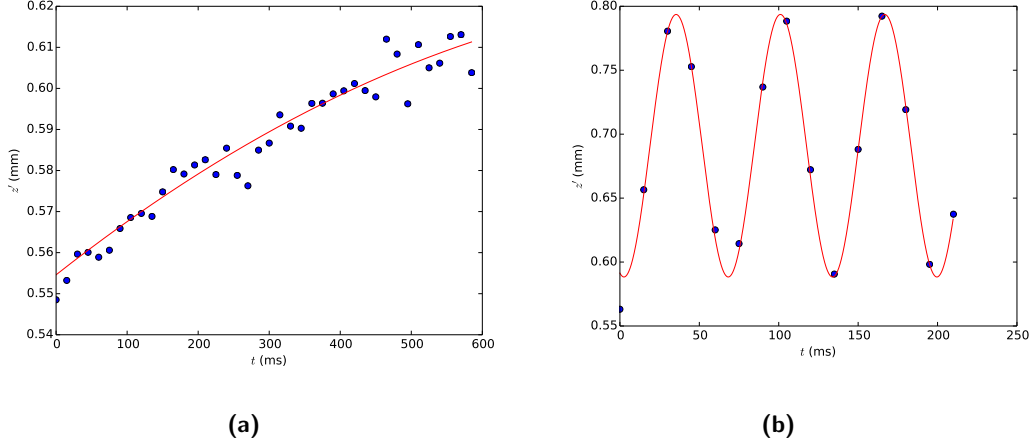
(a) (b)

Figure 3.3: The z'-position plotted as a function of time for typical runs. The blue points indicate the position data as obtained from fits, where the angle between imaging and BEC axis was taken into account. The red lines indicate the best fits done to the position to determine the maximum velocities. (a) shows the displacement due to the slow current ramp with $v_{\max} = 0.14 \pm 0.03$ mm/s and (b) shows the displacement due to the fast current ramp with $v_{\max} = 9.8 \pm 0.3$ mm/s.

Figure 3.4 shows the additions made to the setup to create the repelling barrier. The green laser is situated on a separate optical table. The laser passes through a telescope to size down the beam, an acousto-optic modulator (AOM), a shutter and is coupled into a single-mode fiber. The beam is transferred to the main experimental setup using this fiber. The beam passes a telescope to increase the beam width, and a normal and a cylindrical lens. The focus of the $f = 70$ cm lens lies on the atomic cloud. The cylindrical lens images the beam in one direction and does not effect the light in the other direction. In this way, a line focus is created on the centre of the atomic cloud. The line focus is perpendicular to the z'-axis of the atomic cloud.

In our experiment, the laser power going into the experimental chamber was approximately 370 mW, and the beam waist of the line focus focus was approximately 57 μm and 795 μm in the focussed and imaged direction, respectively. This results in a barrier height of $U/h \approx 4.5$ kHz, which is higher than the typical chemical potential.

3.4 Overview of the Experiments

For this work, five experiments are done. In every experiment, a bimodal atomic cloud was created with temperature below T_c. For each experiment, approximately 20 runs are done. Each atomic cloud was cooled to varying initial chemical potential and temperature. The initial chemical potential was determined to be between 3.0 kHz to 4.1 kHz and the initial temperature was determined to be between 400 nK and 850 nK. For every run, 40 PCI images are taken with 15 ms time intervals. For each
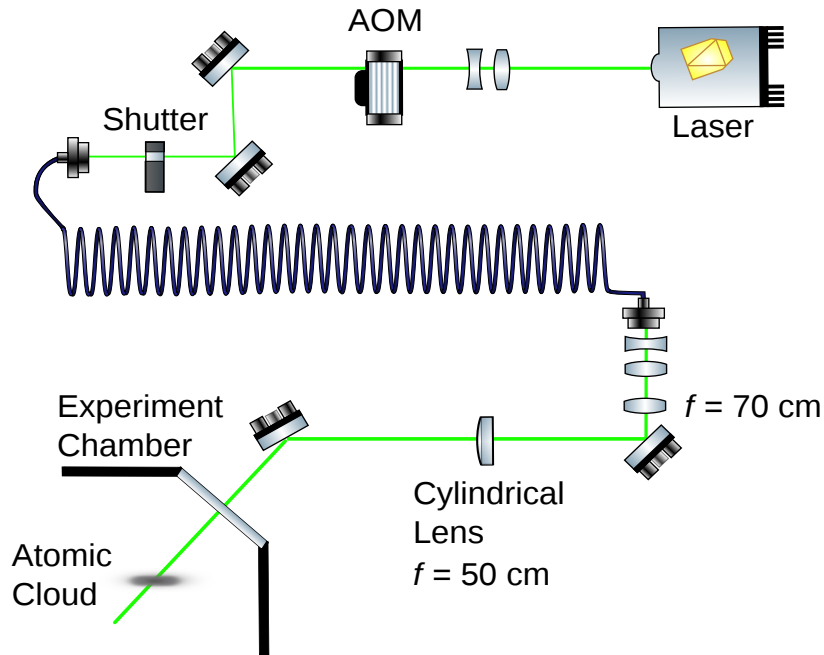
Figure 3.4: Schematic overview of the additions to the setup to shine a line focus on the centre of the BEC.

image, the fitting procedure described in Sec. 3.1 was applied. The time dependence of the chemical potential and the temperature was found for different initial values.

In the first experiment, the stationary experiment, the atomic cloud was not moved and the green laser was not shone on the cloud. The goal of this measurement was to determine the normal temporal behaviour of the chemical potential and temperature of the cloud such that a comparison can be made with the different experiments.

In the second experiment, the slow motion experiment, the atomic cloud was subject to the slow current ramp as described in Sec. 3.2. The slow current ramp was initiated right before the first image. Due to a delay in the response time of the cold atoms, the effect of this motion only becomes visible in the second image. It was estimated that the atoms started moving approximately 10 ms after initiating the ramp. The entire ramp duration was 500 ms.

In the third experiment, the slow motion with laser experiment, the atomic cloud was subject to the slow current ramp exactly like described for the second experiment and in addition the green laser was shone on the cloud. The potential barrier created by the green laser line focus is described in Sec. 3.3. The laser was switched on between the first and second image. In this way, when the first image is taken, the system is unaffected by the change in magnetic field and the laser potential.

In the fourth experiment, the fast motion experiment, the atomic cloud was subject to the fast current ramp as described in Sec. 3.2. Similarly to the second experiment, the ramp was initiated right before the first image was taken. The effect of this change in current only became visible in the second image. The ramp time was $25\,\text{ms}$.

In the fifth experiment, the fast motion with laser experiment, the atomic cloud was subject to the fast current ramp exactly like described for the fourth experiment and in addition the green laser was shone on the cloud in the same way as in the third experiment.

4 Results

The experimental results for the five experiments are discussed in this chapter. The time dependence of the chemical potential and the temperature is measured in five experiments and these results are discussed in Sec. 4.1 through Sec. 4.5. A comparison between the time dependences for the different experiments is given in Sec. 4.6

4.1 The Stationary Experiment

Figure 4.1 shows a typical series of measurements of a single cloud at the times indicated in the upper left corner. The condensate is present in Fig. 4.1a through Fig. 4.1d, which can be observed by a sharp increase in the signal. On the edge of the condensate, the signal rises quickly. As seen in Sec. 2.6, the signal is related to the phase and the phase is proportional to the column density. Examining Eq. 2.21 we notice that the column density of the condensate changes quickly on the edge. Furthermore we notice that the central density decreases over time.

The thermal cloud can best be observed in the diffuse orange cloud off-centre. In this experimental run, the size of the thermal cloud increases over time. Examining Eq. 2.15 we see that a broader thermal cloud indicates an increase in temperature.
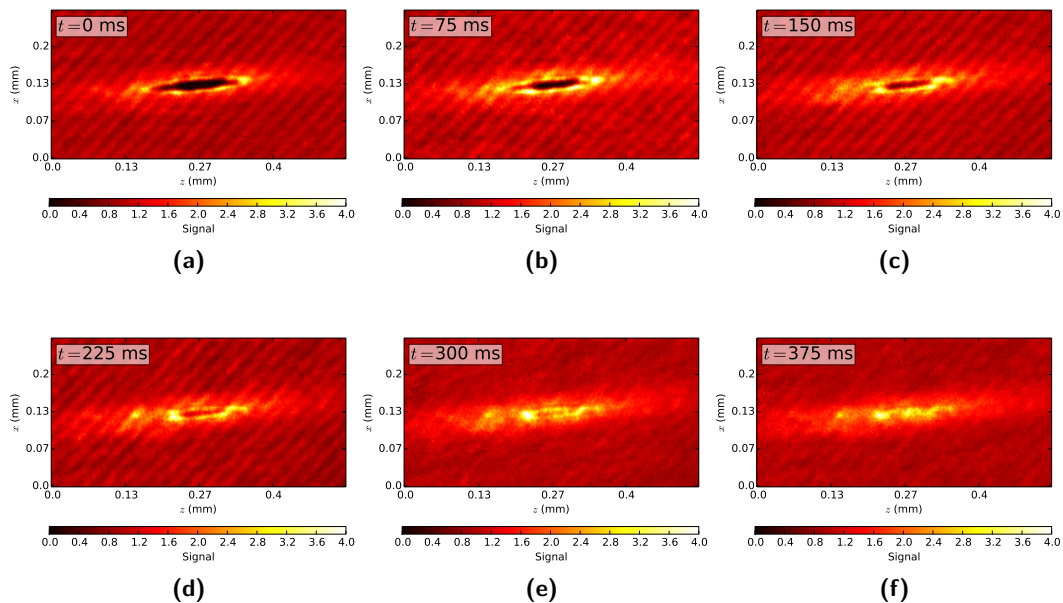

Figure 4.1: Typical measurement series of a single stationary cloud. On the horizontal axis, the imaged z-direction is plotted, on the vertical axis, the imaged x-direction is plotted and the colour bar indicates the signal height. The six figures show the cloud at different times as indicated in the upper left corner.

The fitting procedure as described in Sec. 3.1 was applied to every PCI image. Some fits were rejected on the criteria explained in that section. The condensate fraction generally decreases in time. In some runs, the condensate is gone before the end of the measurement. As soon as the condensate disappeared, the chemical potential becomes negative and the fits are rejected. However, this did not cause any problems since the goal was to study the temporal behaviour of the atomic cloud for temperatures below T_c.
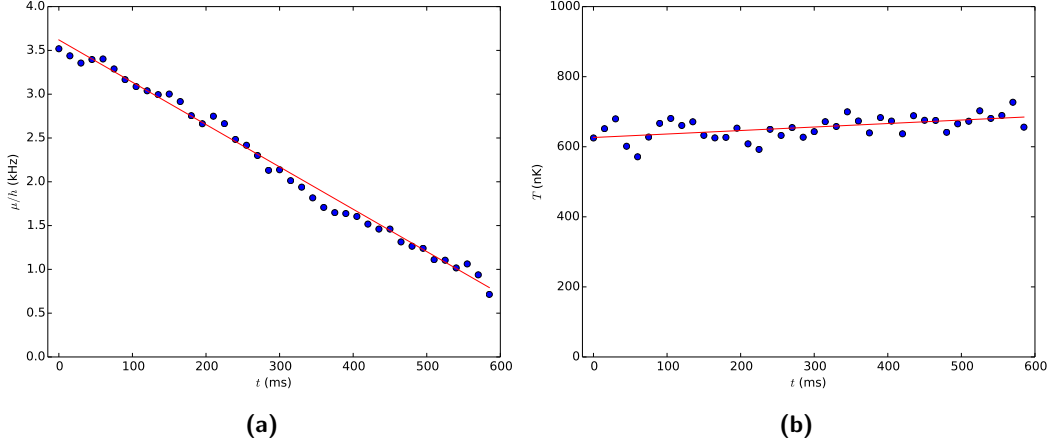
Figure 4.2: (a) and (b) show the chemical potential and temperature, respectively, as a function of time for a typical stationary experiment. The blue points indicate the data and the red lines indicate the best fit to the data. The relative fitting errors in the chemical potential and temperature are smaller than 1% and are smaller than the point sizes.

Figure 4.2 shows the time development of the chemical potential and temperature for a typical stationary experiment. The data is obtained by fitting PCI images as described in Sec. 3.1. In this run, the chemical potential decreases and the temperature increases.

The chemical potential is seen to decrease in time for all runs. The temperature is seen to either increase or decrease in time, which is identified as heating or cooling of the system, respectively. For all runs the chemical potential and temperature were seen to change approximately linearly in time. Therefore, in order to describe the time-development of the chemical potential and temperature, a linear fit was made. These fits described the data well for all PCI images that were accepted. The best fitted value of the slope was identified as $\mathrm{d}\mu/\mathrm{d}t$ and $\mathrm{d}T/\mathrm{d}t$ for the chemical potential and temperature, respectively. The intersection with the y-axis was identified as the initial chemical potential μ_0 and the initial temperature T_0 at the start of the experiment at $t = 0\,\mathrm{ms}$. The two parameters of the fit thus uniquely describe the behaviour in time of the quantity.

For all runs, the chemical potential and temperature were determined and the early

time dependence was modelled by this linear fit. The two fitted parameters of these fits are plotted in Fig. 4.3. We observe that the higher the initial chemical potential, the more negative the time derivative of the chemical potential. The three points in the lower left corner are outliers. For the temperature, we observe a heating regime where $\mathrm{d}T/\mathrm{d}t > 0$ and a cooling regime where $\mathrm{d}T/\mathrm{d}t < 0$. For the temperature we see that the system generally cools down if the initial temperature is relatively high, while the system heats if the initial temperature is relatively low. This behaviour changes around 700 nK.
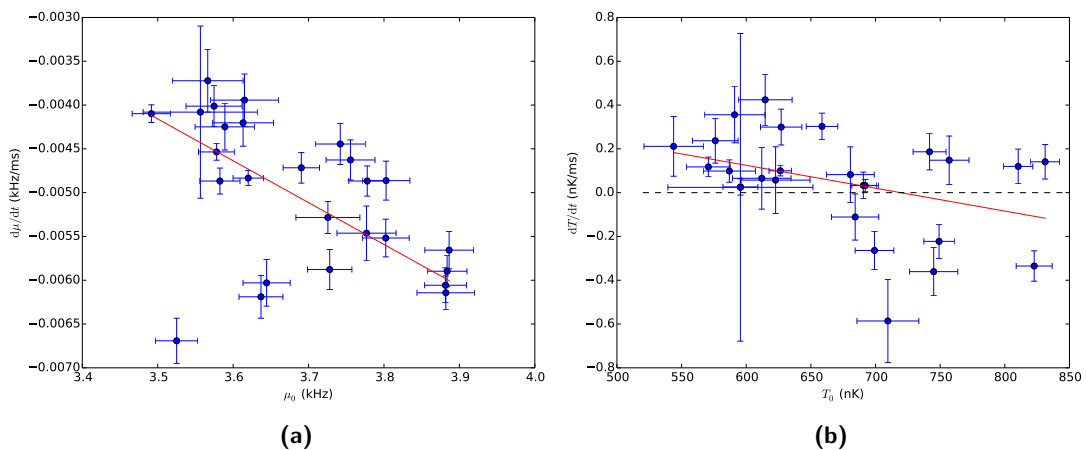

Figure 4.3: (a) shows the time derivative of the chemical potential plotted against the initial chemical potential, (b) shows the time derivative of the temperature plotted against the initial temperature for the stationary experiment. The blue points indicate the best fits to single runs and the error bars indicate the uncertainties in the fitted parameters. The red line indicates the best fit to the data. The dashed black line indicates $\mathrm{d}T/\mathrm{d}t = 0$.

Heating and cooling have been observed in earlier experiments [8]. Two effects take place due to scattering of light on the atoms. On the one hand, atoms gain energy by scattering events. Thermalisation after such events increases the energy of the system. On the other hand, the system can loose energy because atoms are removed from the cloud. If an atom from the condensate is removed, the energy is decreased very little, because the energy of atoms in the condensate is very small. However, if an atom from the thermal cloud is lost, much more energy is lost. An atom from the condensate will take its place, because the chemical potential of the thermal cloud is zero. Since these condensate atoms are much less energetic, the cloud thermalises at a lower temperature. If the first effect dominates, heating is observed, and if the latter effect dominates, cooling is observed.

We notice a strong negative correlation between the initial quantity and time derivative. Therefore the average $\mathrm{d}\mu/\mathrm{d}t$ and $\mathrm{d}T/\mathrm{d}t$ does not describe the behaviour well. Instead, a linear fit was done to this data. A weighted orthogonal distance regression was used to take into account the uncertainties in both directions.

For the chemical potential, the function fitted was $f_\mu(\mu_0) = a_\mu \cdot (\mu_0 - \mu_{\mathrm{tr}})$, where a_μ describes the slope and where μ_{tr} is the transition chemical potential. Based on this simple model, we expect the chemical potential to decrease if μ_0 is above the transition chemical potential, and we expect it to increase if μ_0 is below the transition chemical potential. In this experiment, the latter behaviour is not observed, because the transition chemical potential was determined to be 2.63 ± 0.23 kHz, which is lower than the lowest μ_0 observed in this experiment. Furthermore, a_μ characterises how strongly the time derivative depends on μ_0. In our regime above μ_{tr}, a more negative a_μ means that for given μ_0 the chemical potential will decrease faster in time than for a less negative a_μ. We found for this experiment $a_\mu = -4.8 \pm 1.1 \ \mathrm{s}^{-1}$.

For the temperature, the function fitted was $f_T(T_0) = a_T \cdot (T_0 - T_{\mathrm{tr}})$, where a_T describes the slope and where T_{tr} is the transition temperature. The transition temperature is determined to be 719 ± 35 nK. Below this temperature, heating of the system occurs, and above cooling occurs. a_T quantifies how strongly the time derivative depends on the initial temperature. Above T_{tr}, a large a_T means that heating occurs faster and below T_{tr} this means cooling occurs faster. We found for this experiment $a_T = -1.0 \pm 0.4 \ \mathrm{s}^{-1}$.

Even though this is a simple linear model, it is able to describe the data reasonably well. We expect that the time derivative of our quantities of interest is only a function of the initial quantity. Therefore, for a given initial chemical potential or temperature, we can get an expectation for the short time development of the atomic cloud.

4.2 The Slow Motion Experiment

Figure 4.4 shows a typical series of images at different times taken for the second experiment. At $t = 0$ ms we see a bimodal cloud with a very low signal at the centre of the cloud. Over time, the central signal first increases and after $t = 450$ ms decreases, while the ellipse of maximum signal shrinks. For this run at $t = 450$ ms, the atomic cloud does not show a distinct condensate any more. In addition, we see that the cloud is displaced slowly in the positive z-direction. The shape of the cloud remains unchanged throughout the experiment.

The chemical potential and temperature were found as a function of time for all runs in this experiment. The time development of a typical run is seen in Fig. 4.5. We again note the chemical potential and temperature show approximately linear behaviour in time. The chemical potential decreases, whereas the temperature is seen to increase slightly.

In the same way as for the stationary experiment in Sec. 4.1, our quantifies of interest are analysed by plotting the time derivative against the initial quantity. This is shown in Fig. 4.6. As before, we note that the time derivative of the chemical potential is always negative, and we note either heating of cooling of the system. We again
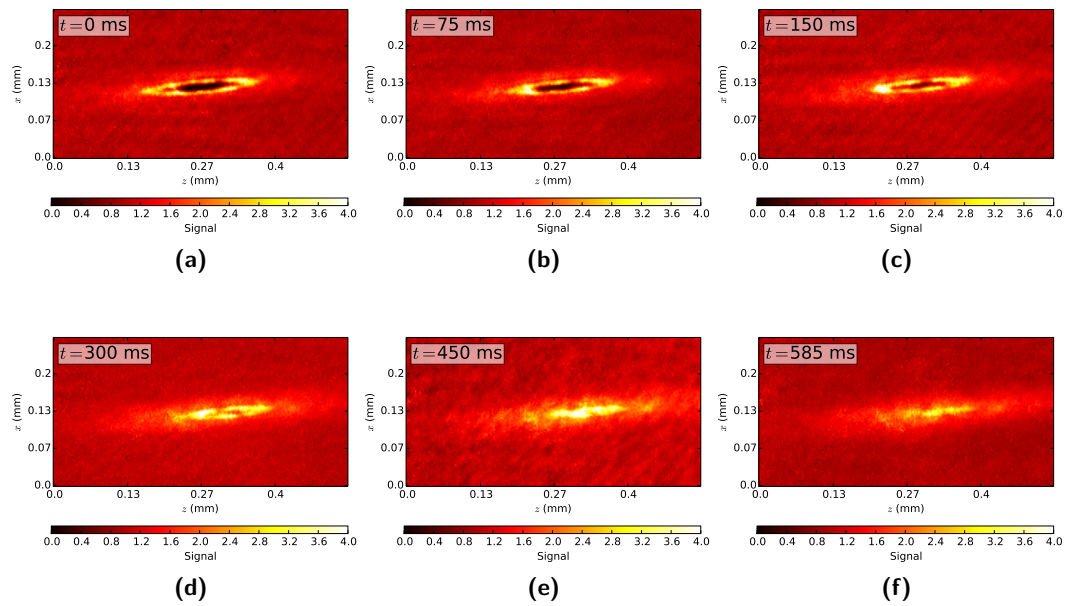
Figure 4.4: Typical measurement series of a single slowly moving cloud. Furthermore, the figure description is the same as in Fig. 4.1.

note a strong negative correlation between these two fitting parameters and describe this by performing a straight line fit as in Sec. 4.1. For this experiment, we find $a_\mu = -5.9 \pm 1.7 \mathrm{s}^{-1}$, $\mu_{\mathrm{tr}} = 2.78 \pm 0.21$ kHz, $a_T = -1.9 \pm 0.5 \mathrm{s}^{-1}$ and $T_{\mathrm{tr}} = 676 \pm 22$ nK.
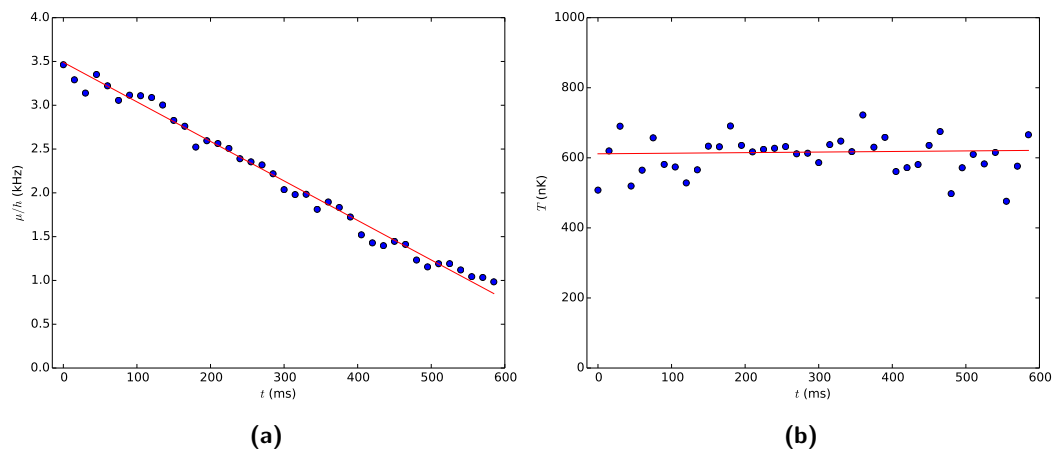

Figure 4.5: Quantities of interest for a typical slow motion experiment. The figure description is the same as in Fig. 4.2.

25

The maximum velocity reached in this experiment is determined to be approximately 0.14 ± 0.03 mm/s, well below the critical velocity. We thus expect the condensate to behave as a superfluid in this regime. Superfluidity is observed if there is no significant difference between the time-development of μ and T. With the analysis presented here, this time-development is described by the four fitting parameters a_μ, μ_{tr}, a_T and T_{tr}. Comparing these four fitting parameters to the fitting parameters of the stationary experiment will thus be enough to conclude if we can observe superfluidity. This will be done in Sec. 4.6.
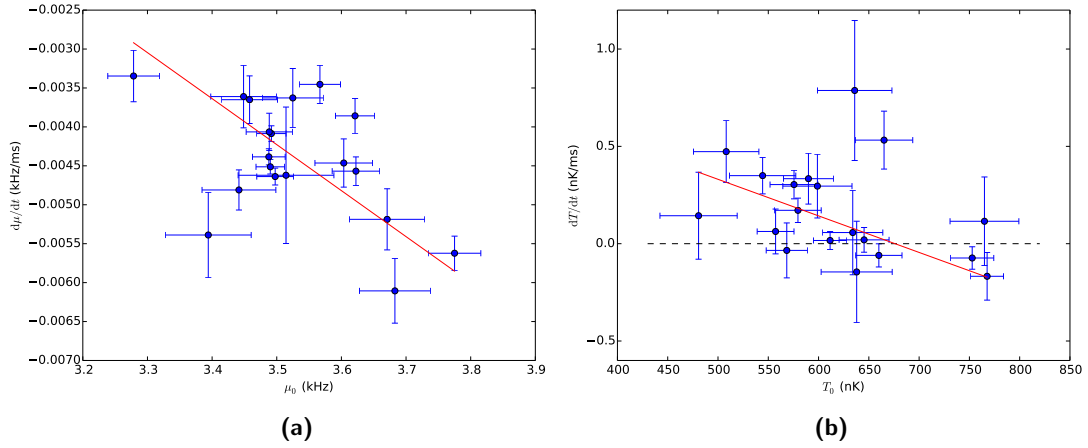

Figure 4.6: The temporal behaviour of the quantities of interest for the slow motion experiment. The figure description is the same as in Fig. 4.3.

4.3 The Slow Motion over Barrier Experiment

In this experiment, the cloud was displaced slowly over a potential barrier, provided by a green laser. Figure 4.7 shows a typical series of images at different times taken for this experiment. A BEC is observed in the centre of the images for all shown times, except the last one. At $t = 375$ ms, the condensate has disappeared and this and later images of this run are therefore not taken into account. In addition, we see that the cloud is displaced slowly in the positive z-direction. The shape of the BEC changes in time in a different way compared to the experiment without the laser barrier. Due to this different shape, the fitting procedure described in Sec. 3.1 was unable to describe the data well. In these cases, the fit was omitted and the next PCI image was found for which the fit gave a good description. At time $t = 150$ ms after the start of the experiment, the data was in general described well by our model. Note that the first image looks the same as a stationary cloud. The first image was always described well by our model.

We note that the effect of the motion and laser only becomes visible in the second

image. The laser is aimed approximately at the centre of the stationary cloud. In the second image, the condensate has moved very swiftly to the right of the barrier. This is as we expect. The laser was aimed at the centre of the BEC, but the centre of the magnetic trap is displaced to the right in the second image. The minimum of the total external potential is therefore at the right of the barrier. Looking at the images, the thermal cloud is displaced, but seems unaffected by the laser.
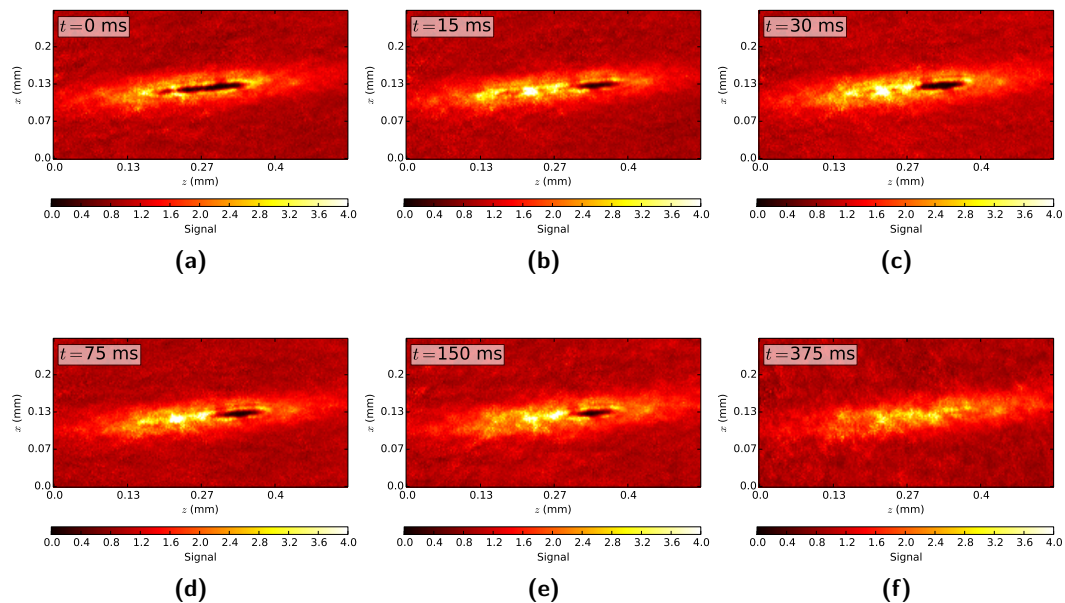

Figure 4.7: Typical measurement series of a single cloud in the third experiment. Furthermore, the figure description is the same as in Fig. 4.1.

Figure 4.8b shows typical results for the chemical potential and temperature as a function of time. Between 15 ms and 135 ms, the images are not described properly by our fitting procedure, so these were not taken into account. Furthermore note that from 300 ms on, the images were not described well by the fits and therefore these images were also not taken into account. Still, we notice that the time development is approximately linear. Therefore, the same procedure as described in Sec. 4.1 was followed and the time derivatives and initial quantities were found.

Using this procedure, we cannot say anything explicitly about the way the chemical potential and temperature develop between 15 ms and 135 ms. However, we can study the development *after* the interaction with the laser. Since we want to study the effect of the laser, it is sufficient to look at the chemical potential and temperature before and after the laser interaction.

As for the previous experiments, the fitted values for the time derivatives and the initial values of our quantities of interest were plotted. This can be seen in Fig. 4.9.
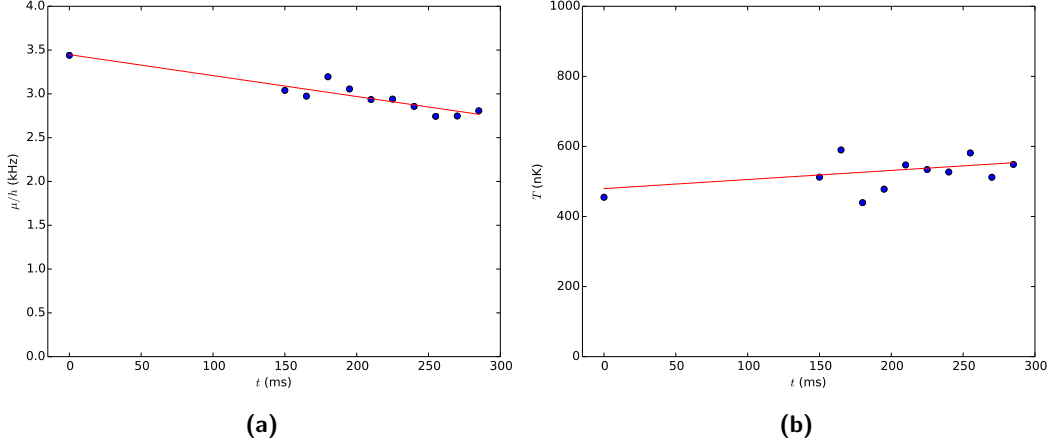
(a)   **(b)**

Figure 4.8: Quantities of interest for a typical slow movement over the barrier experiment. The figure description is the same as in Fig. 4.2. In addition, the second through ninth measurement of the run were not taken into account because the fits to these PCI images were rejected. Note that this example is not the same run as Fig. 4.7.

The time derivative of the chemical potential is negative everywhere, indicating that the chemical potential decreases in time for all runs. Again, the system either heats or cools. Like before, a strong correlation is observed, especially in the chemical potential. To characterise the time behaviour of the chemical potential and the temperature a fit was made. This was done in the same way as described in Sec. 4.1. The best fitted values found here are $a_\mu = -4.2 \pm 0.8$ s^{-1}, $\mu_{\mathrm{tr}} = 2.77 \pm 0.10$ kHz, $a_T = -1.8 \pm 0.4$ s^{-1} and $T_{\mathrm{tr}} = 642 \pm 29$ nK.

Since the current of the MOT coils is ramped in the exact same way as for the second experiment, we can assume we move the cloud by the same velocity that was found for that experiment. For this experiment, we still expect to be in the superfluid regime.

4.4 The Fast Motion Experiment

Figure 4.10 shows a series of PCI images for a typical run of the fast motion experiment. Here, the fast current ramp was applied as explained in Sec. 3.4. We notice a relatively large motion over time, as the centre of the cloud oscillates around a new centre. We see a bimodal cloud for all times plotted. The shape of the condensate and thermal cloud seem to be the same as for a stationary cloud.

The chemical potential and temperature are plotted as a function of time in Fig. 4.11 for a typical run. As in earlier experiments, the time development is approximately linear. This is again described using a linear fit, from which we obtain the time
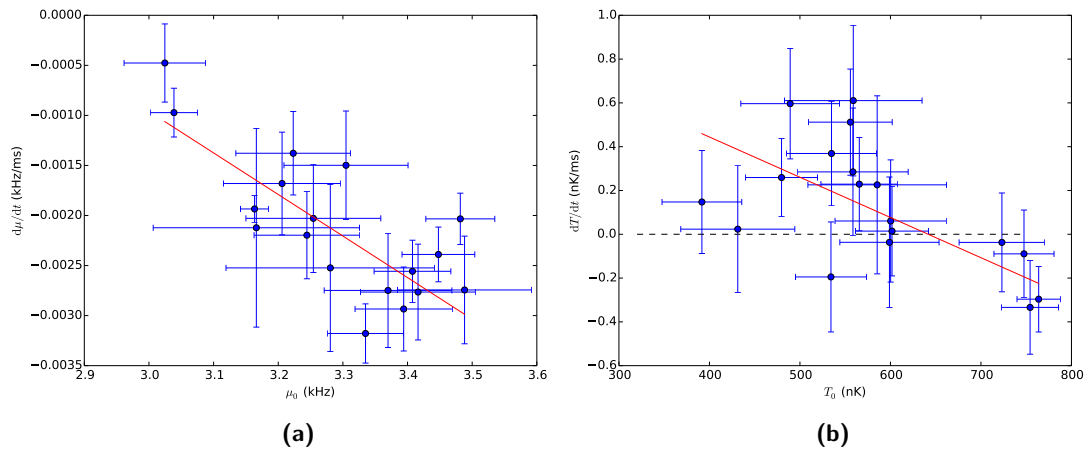
28

Figure 4.9: The temporal behaviour of the quantities of interest for the slow motion over the barrier experiment. The figure description is the same as in Fig. 4.3.
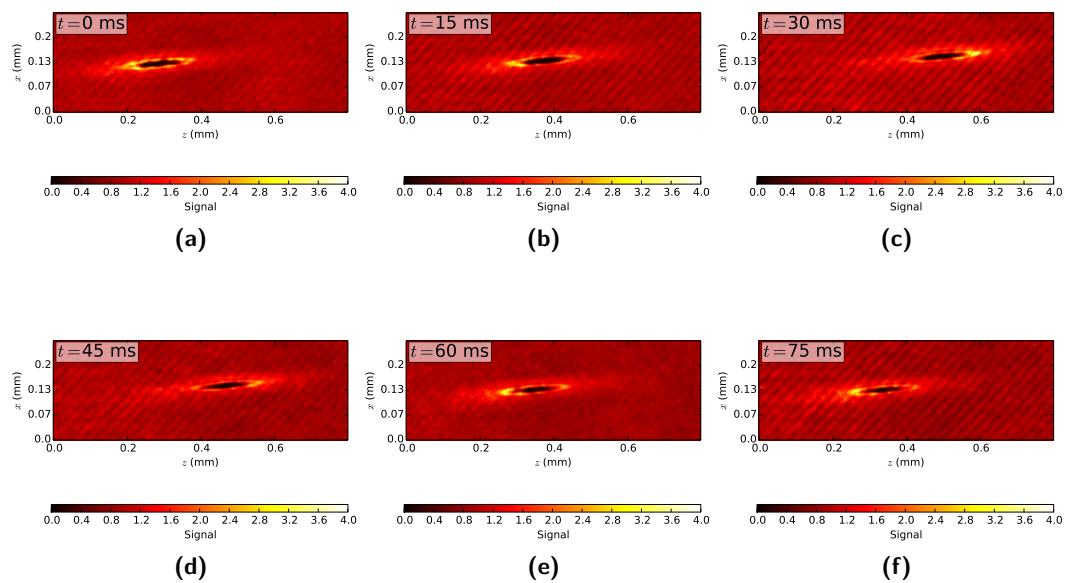

Figure 4.10: Typical measurement series of a single quickly moving cloud. Furthermore, the figure description is the same as in Fig. 4.1.

derivatives and the initial values of the chemical potential and temperature.

Figure 4.12 shows the time derivatives versus the initial values of the chemical potential and temperature as obtained from the linear fits. The time derivative of the chemical potential is negative everywhere, indicating that the chemical potential
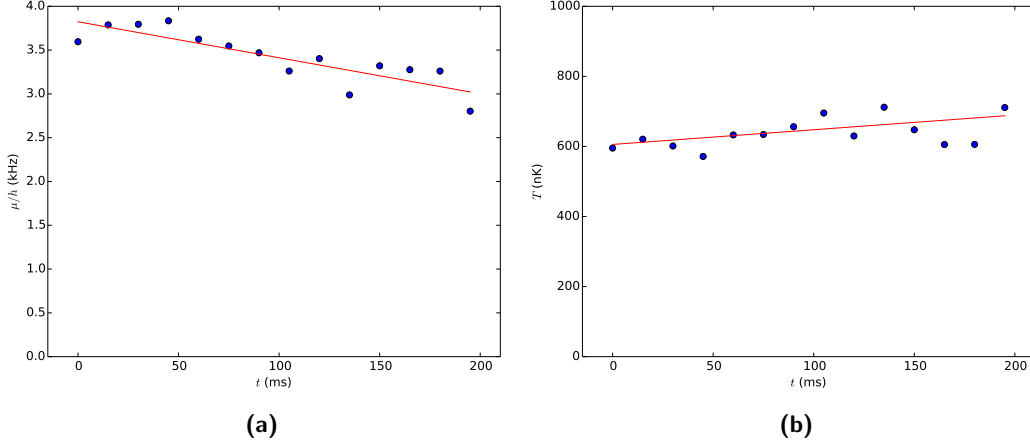
29

Figure 4.11: Quantities of interest for a typical fast motion experiment. The figure description is the same as in Fig. 4.2.

decreases over time for all runs. Again, the system either heats or cools. Like in previous experiments, a strong correlation between the time derivative and initial value is observed, especially in the chemical potential. Therefore, a linear fit was done to characterise the temporal behaviour of the chemical potential and temperature. The best fitted values found for this experiment are $a_\mu = -9.7 \pm 1.3$ s^{-1}, $\mu_{\mathrm{tr}} = 3.29 \pm 0.04$ kHz, $a_T = -4.9 \pm 1.8$ s^{-1} and $T_{\mathrm{tr}} = 663 \pm 28$ nK.
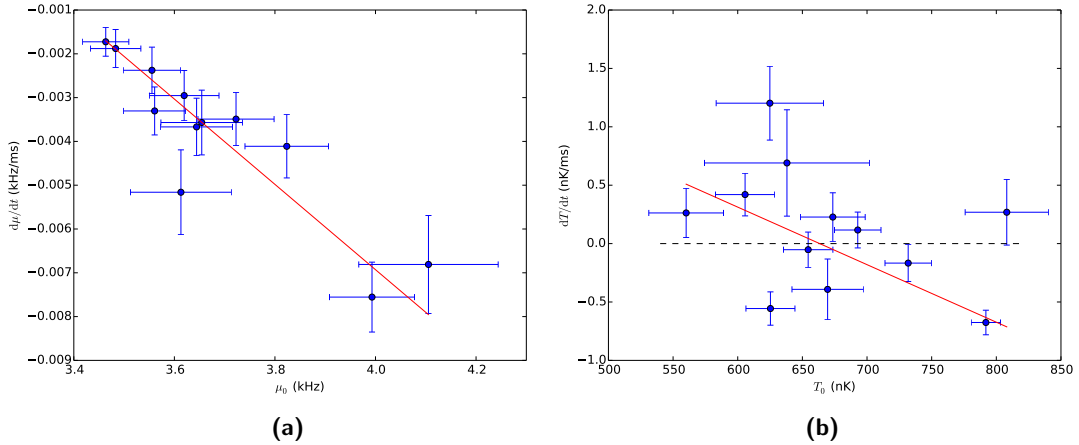

Figure 4.12: The temporal behaviour of the quantities of interest for the fast movement experiment. The figure description is the same as in Fig. 4.3.

The maximum velocity reached in this experiment is determined to be approximately 9.8 ± 0.3 mm/s, well above the critical velocity. We thus do not expect the condensate

30

to behave as a superfluid in this regime, and we expect the chemical potential and temperature to develop differently in time compared to superfluid experiments.

4.5   The Fast Motion over Barrier Experiment

For the fifth experiment, the atomic cloud was moved quickly and in the same way as the fourth experiment. In addition, the laser was shone on the centre to provide a potential barrier. Figure 4.13 shows PCI images at different times. At $t = 0$ ms, the atomic cloud looks like the cloud in a stationary experiment. After initiating the slow current ramp and switching on the laser, the cloud starts to deform and the BEC is forced over the barrier at $t = 15$ ms. At this time, the shape cannot be described well by the fitting procedure. At $t = 30$ ms, the cloud looks normal again. The central density of the cloud is so high that the signal goes back to zero and goes back up again (this is the small orange 'hill' in the middle of the black 'crater'). For later times, the cloud again oscillates. A condensate and thermal cloud are seen everywhere.
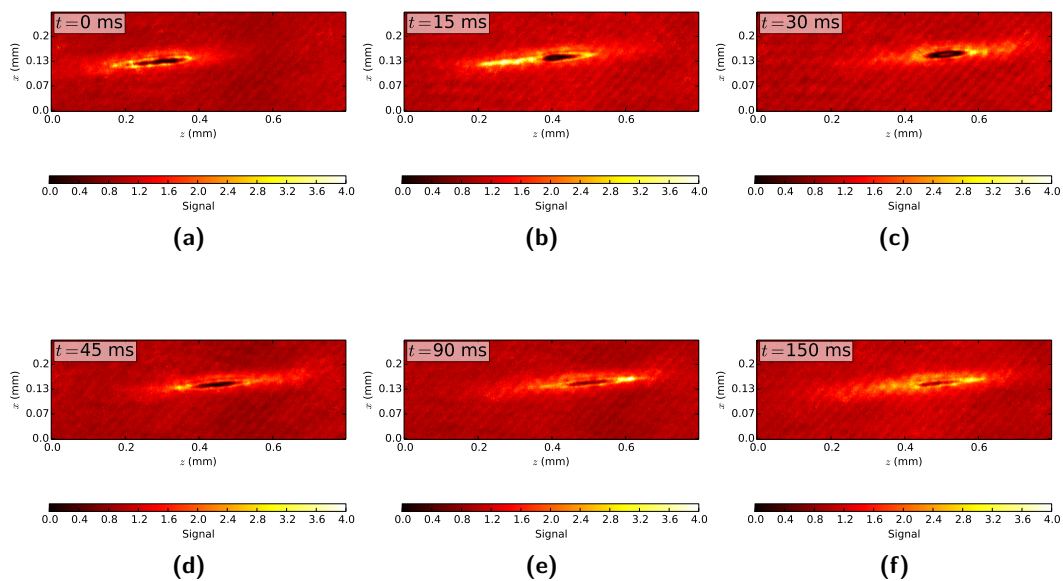

Figure 4.13: Typical measurement series of a single cloud in the fifth experiment. Furthermore, the figure description is the same as in Fig. 4.1.

The same procedure was followed as before. A straight line was fitted to the chemical potential and temperature as a function of time, which described the data well. This can be seen in Fig. 4.14 for a typical run. The time derivative and initial value of μ and T were obtained in this way. These two parameters were plotted against each other in Fig. 4.15. Again we note that $\mathrm{d}\mu/\mathrm{d}t$ is always negative and therefore the
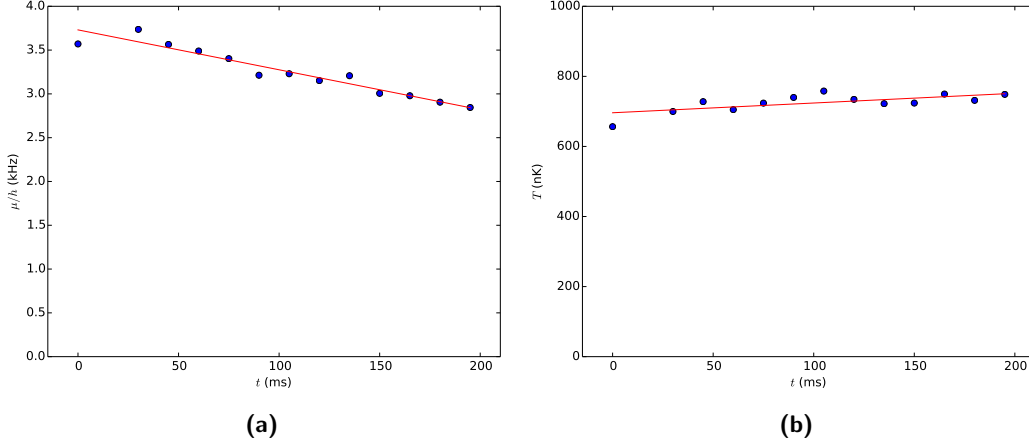
Figure 4.14: Quantities of interest for a typical fast movement over a barrier experiment. The figure description is the same as in Fig. 4.2. The second measurement of the run was not taken into account because the fit to this PCI image was rejected.

chemical potential always decreases over time for our observations. Unlike earlier experiments, the temperature always increases, and cooling is observed in none of the runs. As for the previous four experiments, we see that there is a strong negative correlation between the initial value at $t = 0$ ms and the time derivative. The correlation in temperature is not strong, but a trend is visible. To quantify this, and to compare the temporal behaviour with other experiments, a straight line fit was done again, exactly like described in Sec. 4.1. The best fitted values found for this experiment are $a_\mu = -8.4 \pm 1.7\ \mathrm{s}^{-1}$, $\mu_{\mathrm{tr}} = 3.23 \pm 0.09$ kHz, $a_T = -0.8 \pm 0.5\ \mathrm{s}^{-1}$ and $T_{\mathrm{tr}} = 1.04 \pm 0.27\ \mu\mathrm{K}$. The temperature parameters have a large relative uncertainty because the correlation in the temperature data is not strong.

4.6   Comparison of the Experiments

Table 4.1 shows the four fitting parameters that describe the temporal behaviour of the chemical potential and temperature for each experiment. These parameters quantify how the time derivative of the quantity changes as a function of the initial quantity.

Comparing the a_μ, μ_{tr}, a_T and T_{tr} parameters of the different experiments, we can conclude whether the time development of the experiments is different. Figure 4.16 shows a comparison between the a_μ and μ_{tr} parameters of the five different experiments. We notice that the results of the stationary, the slow motion and the slow motion with laser experiment yield results that are not significantly different from each other. However, the two fast motion experiments are significantly different
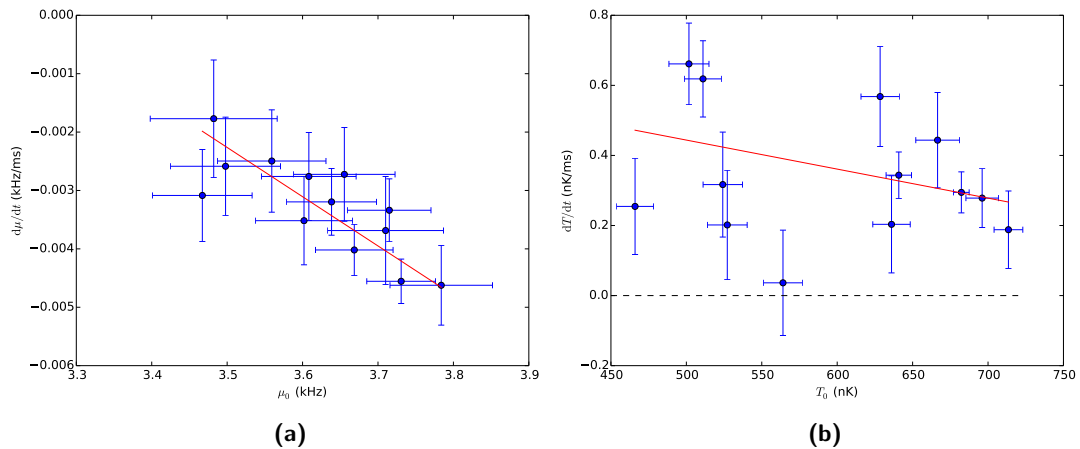
Figure 4.15: The temporal behaviour of the quantities of interest for the fast movement over the barrier experiment. The figure description is the same as in Fig. 4.3.

Experiment	a_μ (s^{-1})	μ_{tr} (kHz)	a_T (s^{-1})	T_{tr} (nK)
1) Stationary cloud	-4.8 ± 1.1	2.63 ± 0.23	-1.0 ± 0.4	719 ± 35
2) Slow movement	-5.9 ± 1.7	2.78 ± 0.21	-1.9 ± 0.5	676 ± 22
3) Slow and laser	-4.2 ± 0.8	2.77 ± 0.10	-1.8 ± 0.4	642 ± 29
4) Fast movement	-9.7 ± 1.3	3.29 ± 0.04	-4.9 ± 1.8	663 ± 28
5) Fast and laser	-8.4 ± 1.7	3.23 ± 0.09	-0.8 ± 0.5	1036 ± 267

Table 4.1: The best fitting values describing the time development of the chemical potential and temperature for the different experiments.

from the stationary experiment. No significantly different temporal behaviour of the chemical potential in the fourth and fifth experiment is observed.

The behaviour can be explained by assuming superfluid flow. Since the two slow motion experiments were done with velocities well below the critical velocity, we expect the system to show superfluidity. This implies that also the temporal behaviour of the chemical potential is not different compared to a stationary experiment. This is exactly what we observe. Introducing a barrier also does not change the temporal behaviour of the chemical potential significantly, even though the barrier height of ~ 4.5 kHz is higher than our typical chemical potential. This is also what is expected.

For the two fast experiments, the maximum velocity was well over the critical velocity. We thus expect that in these two experiments, excitations are produced, which is expected to lead to a larger decrease in chemical potential over time. We observe this as a_μ is significantly more negative for these fast experiments. Furthermore the transition chemical potential changes. However, since μ_{tr} for all experiments is outside of the region in which the initial chemical potential is measured, we cannot
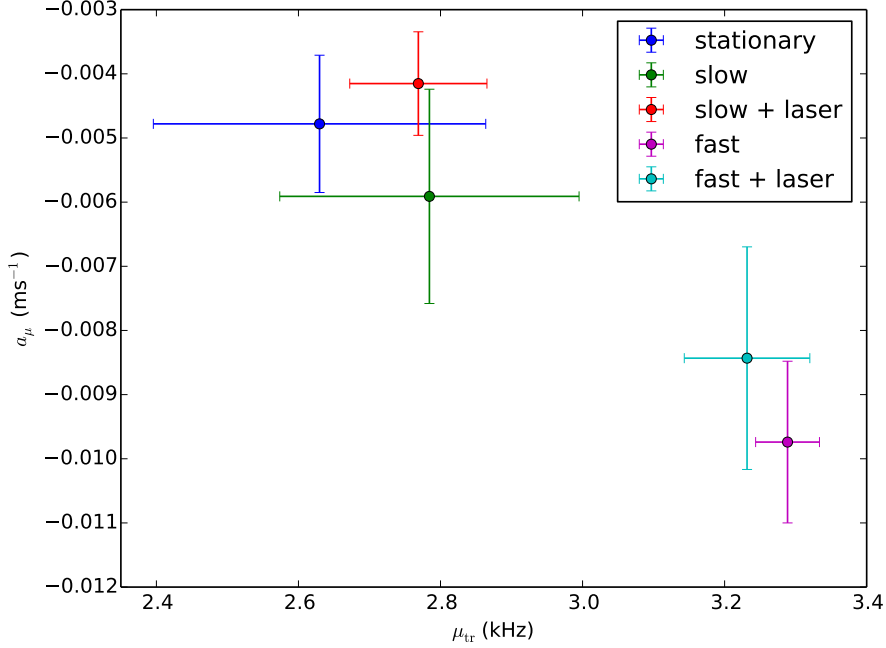
Figure 4.16: The a_μ parameter plotted against the μ_{tr} parameter for the five experiments. The data points give the best estimates of the parameters and the error bars give the statistical uncertainty in the estimate.

say with certainty that this model still holds for values close to and below μ_{tr}.

Figure 4.17 shows the comparison of the temperature parameters. Similar to the chemical potential, we observe that the two slow motion experiments and the stationary experiment do not differ significantly. The two slow motion experiments also do not differ significantly from each other. This can again be explained by superfluidity as discussed for the chemical potential.

The behaviour of the fast motion experiment is significantly different from the stationary experiment. While the transition temperatures are approximately the same for both experiments, the a_T parameter is significantly lower. This indicates that for $T < T_{\mathrm{tr}}$ heating is increased. This is also what we expect, since this experiment has a maximum velocity larger than the critical velocity. Therefore, excitations can be created which leads to increased heating. However for $T > T_{\mathrm{tr}}$ this implies that cooling of the cloud is increased. This is unexpected, but as we see in Fig. 4.12b the runs where cooling is observed are very close to constant temperature. Therefore, we doubt if this model predicts the behaviour above T_{tr} well. A more elaborate model is likely necessary to describe the behaviour above T_{tr}.

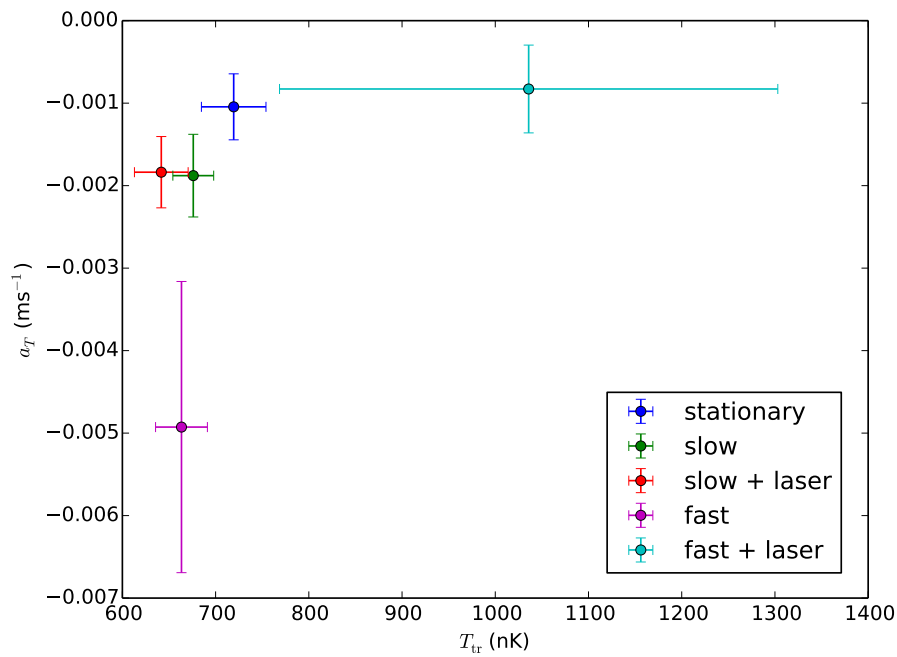The fast motion with laser experiment has a much larger transition temperature

34

Figure 4.17: The a_T parameter plotted against the T_{tr} parameter for the five experiments. The data points give the best estimates of the parameters and the error bars give the statistical uncertainty in the estimate.

than the other experiments, but there is no significant difference from the stationary experiment due to the large uncertainty. However, a higher transition temperature indicates more heating for temperatures below the transition temperature. Looking at Fig. 4.15b we also notice that all runs show heating. More heating is expected, again because the maximum velocity is higher than the critical velocity in this experiment. Therefore, we conclude that the results of this experiment suggest increased heating, but because of the large uncertainties, this cannot yet be asserted conclusively.

5 Conclusion

5.1 Discussion

We have studied the short time development of the chemical potential and temperature in five different experiments. These results will be discussed here.

For the fitting procedure of a single PCI image, many assumptions and approximations are made. Each PCI image is scaled such that the signal at the edges goes to 1, and the signal is set to the theoretical maximum the signal reaches. In addition, a $\theta = \pi/4$ phase spot is assumed instead of the $\pi/3$ phase spot that is used, and in Sec. 3.1 it is shown that this describes the data significantly better. We attribute this deviation in θ to a small misalignment which causes the phase spot to act as a $\pi/4$ instead of $\pi/3$ phase spot. Furthermore, the Bose function in the column density of the thermal cloud is approximated by only taking into account the first two terms. This gives a good approximation because higher order terms give a relatively small contribution. In the theoretical derivation of the column densities, several assumptions are done. We work in the thermodynamic limit, we use the time-independent Gross-Pitaevskii equation and the Thomas-Fermi approximation is applied in the derivation of the BEC column density. Lastly, a non-interacting model is assumed for the total column density.

Using the rejection procedure as explained in Sec. 3.1, we have seen that the fits describe the data very well for bimodal clouds that are not deformed by a laser. We therefore show that the assumptions mentioned before are justified and give a good estimate of the temperature and chemical potential. As the condensate disappears and the temperature reaches T_c, the fitting procedure fails. This is no problem, because we want to study the system below T_c.

Probing of the atomic cloud using PCI leads to particle losses, as described in Sec. 2.6. We have seen that the chemical potential always decreases in our experiments and this indicates that atoms are lost from the condensate. We attribute these losses to the probing of the cloud. In the thermal cloud, we have observed both heating and cooling. In Sec. 4.1 these effects were explained by the interaction of the probe light with the atoms.

The chemical potential as a function of time is fitted with a linear fit for all runs. On longer time scales, the chemical potential shows non-linear temporal behaviour. The temperature as a function of time shows linear behaviour. The fact that we only observe linear time development is attributed to the small time interval we study of clouds well above T_c. Linear fits are done to both the chemical potential and temperature which describe the data well for all runs. In the experiments with the laser barrier, one or more PCI images between $t = 15$ ms and $t = 150$ ms are not taken into account, because they are rejected in the fitting procedure. However,

we still observe the linear time development of μ and T and therefore it is valid to continue and compare the fitting parameters.

Per experiment, the time derivative is plotted against the initial value of the quantity of interest, such as in Fig. 4.3. In most of these plots, a strong negative correlation is observed between the two parameters. A linear fit is done to describe the time development of the quantity of interest. In some of the temperature plots, the correlation is less strong, such as in Fig. 4.15b. We choose to fit by the same procedure to enable comparison between the experiments. Further experiments or simulations must be done to better understand this. However, fitting a straight line gives an interesting first estimate. We note that the uncertainties in the best fitted values are larger for experiments with a weak correlation than for experiments with a strong correlation. Taking into account the uncertainties of the fitted values thus still allows us to give a fair comparison between the experiments.

In the chemical potential and temperature, we have observed superfluidity for the two slow motion experiments. The fast motion experiment shows significantly different temporal behaviour in the chemical potential and temperature. In the fast motion experiment, additional heating of the system is observed. In the fast motion experiment with the laser, we observe increased heating, but the deviation from the stationary experiment is not significant due to the large uncertainty in T_{tr}.

Even though the time development of the temperature in a fast motion with laser experiment is not significantly different from a stationary experiment, we note it is significantly different from the fast motion experiment without laser. In the chemical potential a significant difference between the fast experiment with laser and the stationary experiment is observed. Therefore, we conclude that overall the temporal behaviour of the fast motion experiment is significantly different from both the stationary experiment *and* the other fast experiment, while the fast experiment with the laser barrier is also significantly different from the stationary and the fast motion experiments.

Our analysis of the temporal behaviour of the chemical potential predicts a transition chemical potential below which the chemical potential increases, rather than decreases. This is not observed in the experiments, because the atomic clouds are always prepared in the regime with $\mu_0 > \mu_{\text{tr}}$. We do not expect that the chemical potential increases over time for these experiments. Rather, this linear description is valid in the region we studied, and we cannot extrapolate the results. Further research is needed to study this. However, we observe a difference in the transition chemical potential between the fast motion experiments and the slow motion and stationary experiments. This suggests different temporal behaviour in these experiments.

On the other hand, the analysis of the temporal behaviour of the temperature yields results about the transition temperature. These are valid because this transition temperature is in the range of the initial temperatures.

5.2 Conclusions

A fitting procedure is written which is able to describe PCI images of bimodal clouds well. The chemical potential is seen to decrease for all initial values, while the temperature is seen to either increase or decrease, depending on the initial value. In the short time regime that is studied, the time development of both quantities is approximately linear. The chemical potential and temperature as a function of time are fitted, and the time derivatives and initial values are obtained. We have observed a strong correlation in these parameters and a second linear fit is done to the time derivatives and the initial values, yielding two parameters. We have characterised the behaviour of the chemical potential and temperature in time, each by two parameters. This characterises the temporal behaviour of the quantities of interest. Comparing these parameters for the experiments, we conclude that we have observed superfluidity for velocities below the critical velocity, and we have seen indications of additional heating for velocities above the critical velocity.

For the temperature, heating is observed for temperatures below a certain transition temperature. Above this transition temperature, cooling occurs. This transition temperature is found for all experiments. For stationary experiments, we find $T_{\mathrm{tr}} = 719 \pm 35 \, \mathrm{nK}$.

Outlook

To better understand the results, full simulations should be done. This gives insight in the relevant processes and the time development of the chemical potential and the temperature, also during the interaction with the barrier.

The analysis as done in this work, predicts that the chemical potential increases when the initial chemical potential is below a certain μ_{tr}. It is interesting to create a cloud such that this prediction can be checked.

Furthermore it is interesting to study longer time developments. Non-linear behaviour will be observed. Studying the cloud as the condensate disappears also allows the study of the behaviour around T_{c}.

Lastly, it is interesting to replace one of the mirrors in the beam path of the green laser after the fiber by a spatial light modulator. Interesting dynamical experiments can be done, as shown in Refs. [15] and [16]. In addition, the line focus can be shaped accurately. A line focus with a small hole can be created and this can be used to study transport through this hole.

6 Acknowledgements

First of all, I would like to thank my supervisor, Peter van der Straten. This work would not have been possible without him. I really appreciate all the time you took to explain the theory, helped understand the data and interpret the results, and help me forward in general. Your door was always open and I always felt welcome. I really admire your enthusiasm, which surfaces especially when you are helping in the lab, or trying to understand something that looks interesting. It also shows when talking about education. I am glad that I also had the opportunity to work as your assistant in the quantum mechanics course and share thought on education. Working together has taught me a lot and has been a very good experience for me.

The 'Happy Bosons' have also been of great help to me. I would like to thank Jasper for his help in the lab, the good ideas and times you took to explain theory and the lab to me, and the fun times at, for example, the sport's day. Thanks to Qiao for the help in the lab, the useful discussions, and the nice meaty dinners. Broos, thanks a lot for our good cooperation during the first three quarters of the research, the ping pong games and I guess also for the little teapot. At the very beginning of this work, Christian and Pieter made sure that we understood the lab, for which I want to thank them very much.

The work in the lab needed a lot of practical experience, and for this the technical staff was invaluable. Thanks a lot for all the help in the lab Paul, Cees, Dante and Fritz. Without you, I would still have been fiddling with shutters, fibers and electronics right now.

My thanks also goes out to my fellow Master students in the group. Robbert, James, Gordian, Marcel, Jasper C, Karindra, and Anne, we often had interesting and relevant discussions, and you all made this an enjoyable time, also in the time we spend outside of the offices. In specific I want to thank Gordian for all the time he took to help me with programming.

Furthermore, I would like to thank Dries for the useful discussions, and the interesting discussions on music and much more. And lastly, I would like to thank all the other members of the group. We might not have worked together so much, but it created a great basis for a group that was both helpful and fun.

References

[1] E. A. Cornell and C. E. Wieman, *Nobel lecture: Bose-einstein condensation in a dilute gas, the first 70 years and some recent experiments*, Rev. Mod. Phys. **vol. 74**, pp. 875–893, URL `http://link.aps.org/doi/10.1103/RevModPhys.74.875` (2002)

[2] W. Ketterle, *Nobel lecture: When atoms behave as waves: Bose-einstein condensation and the atom laser*, Rev. Mod. Phys. **vol. 74**, pp. 1131–1151, URL `http://link.aps.org/doi/10.1103/RevModPhys.74.1131` (2002)

[3] C. Pethick and H. Smith, *Bose-Einstein Condensation in Dilute Gases*, Cambridge University Press, 2nd ed. (2008)

[4] J. Klaers, J. Schmitt, F. Vewinger, and M. Weitz, *Bose-einstein condensation of photons in an optical microcavity*, Nature **vol. 468**, pp. 545–548 (2010)

[5] P. van der Straten and H. Metcalf, *Atoms and Molecules Interacting with Light*, Cambridge University Press, 1st ed. (2016)

[6] S. Blundell and K. Blundell, *Concepts in Thermal Physics*, Oxford University Press, 2nd ed. (2009)

[7] W. Ketterle, D. S. Durfee, and D. M. Stamper-kurn, *Making, probing and understanding bose-einstein condensates*, *Proceedings of the International School of Physics "Enrico Fermi", Course CXL, Edited by M. Inguscio, S. Stringari and C.E. Wieman*, IOS Press, pp. 67 – 176 (1999)

[8] P. Bons, *Probing the properties of quantum matter*, Ph.D. thesis, Utrecht University (2015)

[9] R. Meppelink, R. A. Rozendaal, S. B. Koller, J. M. Vogels, and P. van der Straten, *Thermodynamics of bose-einstein-condensed clouds using phase-contrast imaging*, Phys. Rev. A **vol. 81**, p. 053632, URL `http://link.aps.org/doi/10.1103/PhysRevA.81.053632` (2010)

[10] S. Koller, *Experiments on hydrodynamic transport in ultra-cold bose gasses*, Ph.D. thesis, Utrecht University (2012)

[11] R. Meppelink, S. B. Koller, and P. van der Straten, *Sound propagation in a bose-einstein condensate at finite temperatures*, Phys. Rev. A **vol. 80**, p. 043605 (2009)

[12] A. Groot, *Excitations in hydrodynamic ultra-cold bose gases*, Ph.D. thesis, Utrecht University (2015)

[13] R. Grimm, M. Weidemüller, and Y. B. Ovchinnikov, *Optical dipole traps for neutral atoms*, Advances in atomic, molecular, and optical physics **vol. 42**, pp. 95–170 (2000)

[14] C. te Riet, *Spatial non-destructive imaging of spin domains in bose-einstein condensates*, Master's thesis, Utrecht University (2014)

[15] V. Boyer, R. M. Godun, G. Smirne, D. Cassettari, C. M. Chandrashekar, A. B. Deb, Z. J. Laczik, and C. J. Foot, *Dynamic manipulation of bose-einstein condensates with a spatial light modulator*, Phys. Rev. A **vol. 73**, p. 031402, URL `http://link.aps.org/doi/10.1103/PhysRevA.73.031402` (2006)

[16] D. McGloin, G. Spalding, H. Melville, W. Sibbett, and K. Dholakia, *Applications of spatial light modulators in atom optics*, Opt. Express **vol. 11**, no. 2, pp. 158–166, URL `http://www.opticsexpress.org/abstract.cfm?URI=oe-11-2-158` (2003)